The effect of EEG on Assessment of Cerebral Autoregulation

Suresh Kumar Narinahally Krishnamurthy
St Cross College
Trinity Term, 2019

Supervisor:
Prof. Stephen J Payne
Department of Engineering Science

This thesis is submitted for the degree of Master of Science (by Research)

Abstract

Cerebral blood flow (CBF) is determined by vascular resistance, mean arterial blood pressure ($MABP$) and intracranial pressure. The energy requirement of brain cells means CBF has to be maintained constant despite changes in pressures. Cerebral autoregulation is the mechanism which keeps the CBF constant for a range of variations in pressure. Autoregulation can be impaired after stroke, trauma or anaesthesia. Following the impairment of autoregulation, such as under intensive care conditions, previous studies have found that Electroencephalography (EEG) signals also change in their frequency content in a manner that corresponds to decreases in CBF. These studies have suggested that decreasing levels of blood flow change the metabolic and electrical activity of cortical neurons.

Assessment of autoregulation status is essential to help to reduce or to prevent any further damage or cell death. With the availability of techniques to continuously monitor and to record physiological variables such as blood pressure, blood flow rate, it is possible to make continuous assessments of autoregulation. There are many methods to assess autoregulation and the most commonly used methods include transfer function analysis (TFA) and the autoregulation index (ARI) method.

As EEG has the advantage that it can be recorded in real time, it offers the promise of potentially providing an additional non-invasive real time autoregulation assessment, given that we have some understanding of interpreting how exactly changes in EEG reflect the status of blood flow. Though there is strong clinical evidence of the relationship between EEG frequency change and CBF changes there are no model based investigations or methods that could explain the mechanism of how both are coupled.

In order to attempt a study of this link between EEG and CBF, we devised an artificial reduction in CBF levels, by increasing the resistance of large arteries in steps, using an existing haemodynamic model, which is capable of handling simultaneous changes in ABP, $CO2$ and neural input (EEG). We generated CBF using our haemodynamic model, by feeding in experimental data for ABP,$CO2$ and synthetic EEG, for every step reduction in large artery resistance. Using the autoregulation assessment methods TFA and ARI, we studied how the EEG behaviour affects the assessment of autoregulation. Results show that EEG input appears to make autoregulation 'better' by a small fraction under the circumstances of the model and data we have used. There is, however, high variability between different subject data. The implication from this study is that, on average EEG input increases the measure of autoregulation slightly, but the variability between subjects means that more, controlled, data are required to validate fully this study's observations.

Contents

List of Figures

List of Tables

Chapter 1

Introduction

The Human Brain is the most complex organ made up of a network of billions of nerve cells called neurons, and other kinds of cells as well. It functions as the main command centre of the living being. The brain weighs around 2% of body weight, but it receives about 15-20% of total cardiac output, which is required to meet its high metabolic needs. The metabolic demand of the brain is fulfilled by the consumption of oxygen and glucose delivered to it by blood. In turn, this requirement of blood makes the brain the most highly perfused organ in the body. The blood circulation mechanism to brain is called the cerebral circulation. The blood flow through the brain is roughly 800 mL per minute, with approximately 75 mL of blood present within the brain at any given moment (Noback et al., 2005). The brain stores only a minute amount of glucose and oxygen, so it is a necessity that there is a continuous flow of blood. Even if the supply is cut off for less than 10 seconds, consciousness is lost.

1.1 Arterial blood supply to Brain

The arterial blood supply (incoming blood from the heart) to the brain comes from four arteries, the left and right internal carotid arteries and similarly from vertebral arteries. Major network of blood vessels are shown in Fig 1.1. The vertebral

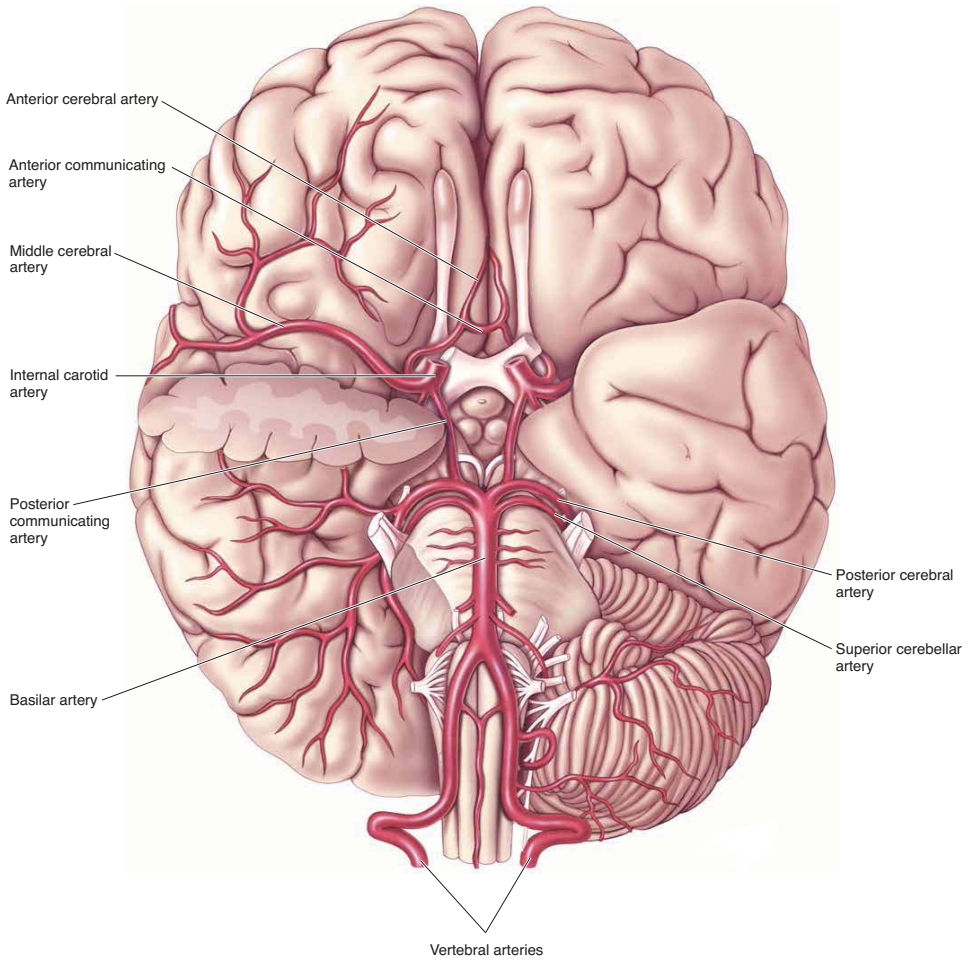

Figure 1.1: Major arterial blood supply to Brain (Bear et al., 2007).

arteries after entering through the skull, unite to form the basilar artery and then supply posterior parts of cerebral hemispheres, through posterior cerebral arteries. The internal carotid arteries after traversing the skull divide into anterior and middle cerebral arteries (MCA). In addition to these at the base of the brain in the circle of willis, communicating arteries offers the potential to maintain cerebral circulation in the event of occlusion (blockage) in any of the major arteries.

1.2 Venous drainage of the brain

The veins draining the brainstem and the cerebellum roughly follow the arterial supply, whereas the veins draining the cerebrum do not follow parallel to arterial trees (Noback et al., 2005). The venous collateral network are extensive and effective

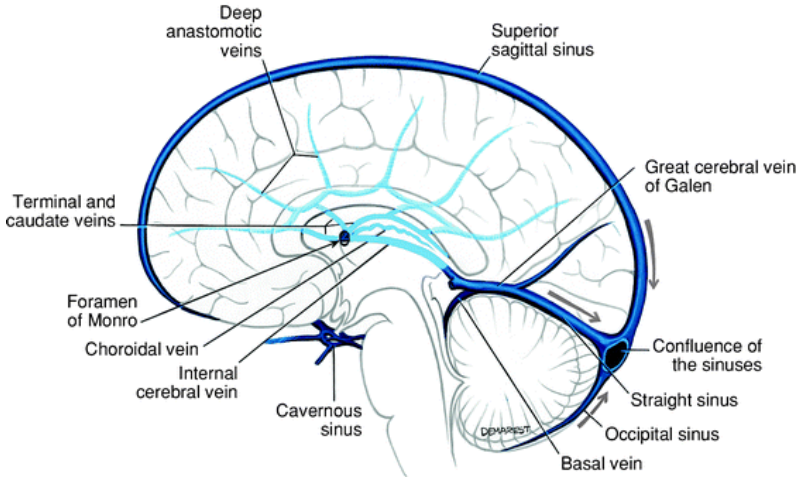

Figure 1.2: Venous drainage from the brain (Noback et al., 2005).

between deep veins within the brain and the superficial surface veins. The internal cerebral veins drain the deep structures of the cerebral hemispheres into the straight sinus. The blood from the upper, lateral and medial parts of the cerebrum drains into the superior sagittal (dural) sinus. A lateral view of the venous drainage is shown in Fig 1.2.

1.3 Cranial cavity

The brain is housed within the cranial cavity, also known as the intracranial space, the space within the skull, which offers bony protection to the brain. Soft brain is protected by meninges, made up of three protective layers. The three layers are the dura mater, a thick tough layer close to the skull; adjacent to dura mater is the arachnoid mater, a thin membrane; and the pia mater, which envelops the brain and spinal cord (Fig 1.3). The subarachnoid space is the space between the arachnoid mater and pia mater, filled with cerebrospinal fluid (CSF). CSF plays an important part in maintaining a constant intracerebral chemical environment. Mechanically CSF protects the brain from sudden movements by buffering the effects of impact. Another protective element is the blood-brain barrier (BBB), which is a barrier between blood vessels and the neural cells and other components of brain tissue.

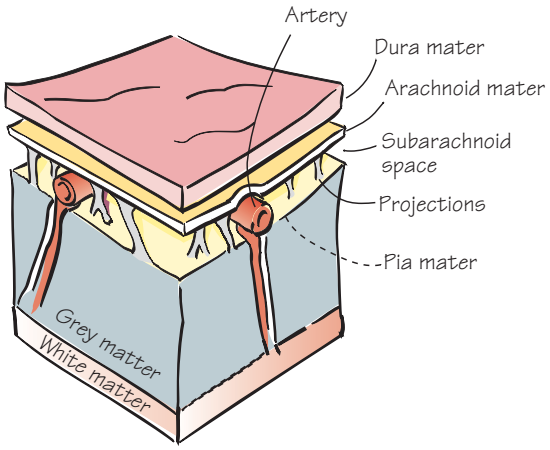

Figure 1.3: Meninges covering the brain (Barker et al., 2017).

It provides a defence against disease causing pathogens and toxins, that might be present in the blood, while allowing vital nutrients to the neural tissue.

1.4 Intracranial Pressure

The intracranial space is composed of three contents, cerebrospinal fluid, cerebral blood and brain tissue. These are almost incompressible, and are enclosed in a non-expandable case of bone, so a change in volume of any one of them has to be compensated for by one or more changes in the other two components. This gives us the following equation (Gonzalez et al., 1994),

$$V_{CSF} + V_{Blood} + V_{Tissue} = V_{total\ intracranial} \tag{1.1}$$

This compensatory mechanism in the intracranial space provides a natural way to maintain a constant total intracranial volume (Gonzalez et al., 1994). As a result the volume of blood in the cranial cavity is nearly constant and for incoming arterial blood a continuous outflow of venous blood is required. The pressure within the intracranial space is termed the intracranial pressure (ICP). The ICP at rest is normally in the range of 7-15 mmHg, while lying flat (Steiner and Andrews, 2006). There are various mechanisms to keep the ICP in its normal range, such as the reduction of the volume

of cerebrospinal fluid or intracranial blood.

1.5 Cerebral Haemodynamics

Cerebral haemodynamics is the study of blood flow in the brain. The equivalent to Ohm's law in relation to blood flow (Q), is defined by the pressure difference ($\triangle P$ termed driving pressure, cerebral perfusion pressure (CPP) or pressure gradient) and the resistance to flow (R) offered by the blood vessel and its interactions with blood. The haemodynamic relationship is given by Eqn 1.2:

$$Q = \frac{\triangle P}{R} = \frac{(P_A - P_V)}{R} \tag{1.2}$$

where P_A is the arterial pressure and P_V is the venous pressure.

Venous pressure is normally low in the range on 2-5 mmHg and is directly influenced by Intracranial pressure (ICP) (Cipolla, 2009). Therefore, $\triangle P$ is can be calculated as the difference between CPP and either venous pressure P_V or ICP whichever is greater.

The cerebral blood flow (CBF) is described by Hagen-Poiseuille equation :

$$CBF = \frac{\pi \triangle P r^4}{8\mu L} \tag{1.3}$$

where $\triangle P$ is the pressure difference driving the blood flow which is CPP, r the radius of blood vessel, μ the dynamic viscosity of blood, and L the length of blood vessel. The radius of the blood vessel is the most powerful determinant of blood flow and any slight changes in diameter will thus have significant effects on the cerebral blood flow.

Cerebral perfusion pressure (CPP) is the difference between mean arterial pressure (MAP) and the intracranial pressure (ICP), given by Eqn 1.4:

$$CPP = MAP - ICP \tag{1.4}$$

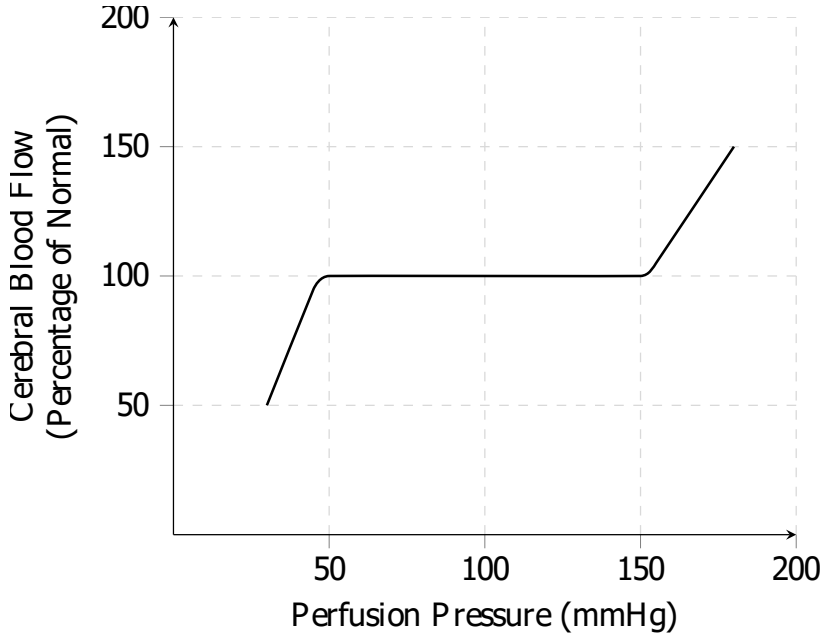

Figure 1.4: Autoregulation curve, CPP vs CBF

1.6 Cerebral Autoregulation

Autoregulation is the ability to regulate and maintain blood flow despite changes in perfusion pressure. In healthy individuals cerebral blood flow (CBF) is autoregulated over the range of approximately 60-160 mmHg mean arterial pressure (MAP). This is shown in Fig 1.4. Above or below this limit the autoregulation is lost and CBF linearly follows MAP.

1.6.1 Mechanisms of Autoregulation

As given by Eqn 1.3 cerebral blood flow can be regulated by varying any of the parameters, but other than the radius of blood vessel, most of them are largely invariant. The regulation of blood flow can thus be considered as merely changing the radius of blood vessel. Different mechanisms exists which act independently or together to alter the vessel radius.

Pressure autoregulation or the myogenic mechanism occurs when there is an increase in MAP. It increases the transmural vessel tension, causing depolarisation of vascular smooth muscles leading to vasoconstriction. Similarly the reverse happens

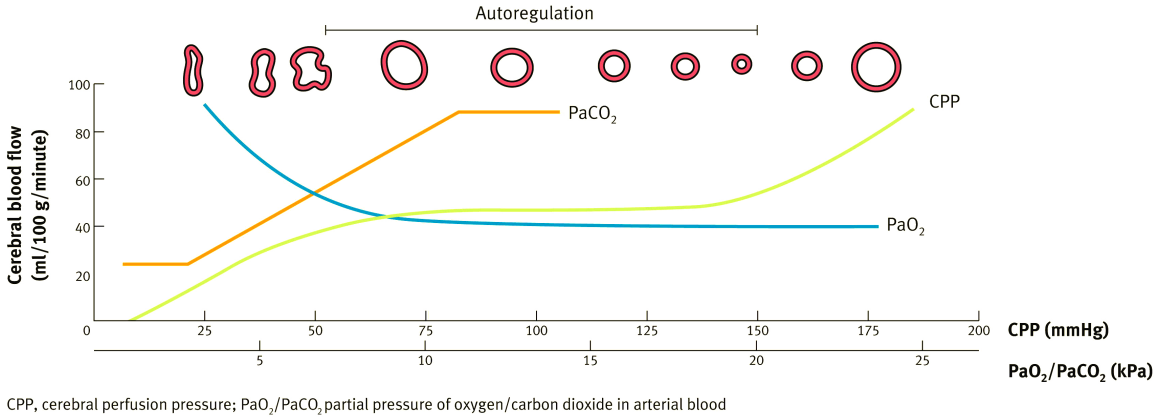

Figure 1.5: Effect of changes in MAP, P_aCO_2 and P_aO_2 (Shardlow and Jackson, 2011)

when MAP, and thereby transmural tension, decreases leading to vasodilation. This process is mediated by endothelium derived relaxing factor and nitric oxide (Tameem and Krovvidi, 2013).

CBF is strongly influenced by blood P_aCO_2 levels (Payne, 2016). An increase in arterial P_aCO_2 causes vasodilation and a decrease in arterial P_aCO_2 causes vasoconstriction. The relationship between P_aCO_2 and CBF is almost linear with plateau at upper and lower levels of approximately 10.6 and 2.7 kPa (Shardlow and Jackson, 2011). Beyond the plateau there is little change in CBF. When blood P_aO_2 decreases, CBF is increased by vasodilation, increasing oxygen will cause vasoconstriction. These effects are shown in Fig 1.5.

Flow-metabolism coupling is one of the major mechanisms that regulate cerebral blood flow at the local level of brain tissue. CBF is normally closely matched to the cerebral metabolic rate for oxygen ($CMRO_2$). An increase in neuronal activity causes an increase in the cerebral metabolic rate, which in turn results in increased CBF. This forms the basis for functional MRI and this coupling is also called the neurovascular coupling. Neurovascular coupling is defined by the anatomical and metabolic relationship between neurons, glial cells and penetrating arterioles, together collectively known as the neurovascular unit (Willie et al., 2014).

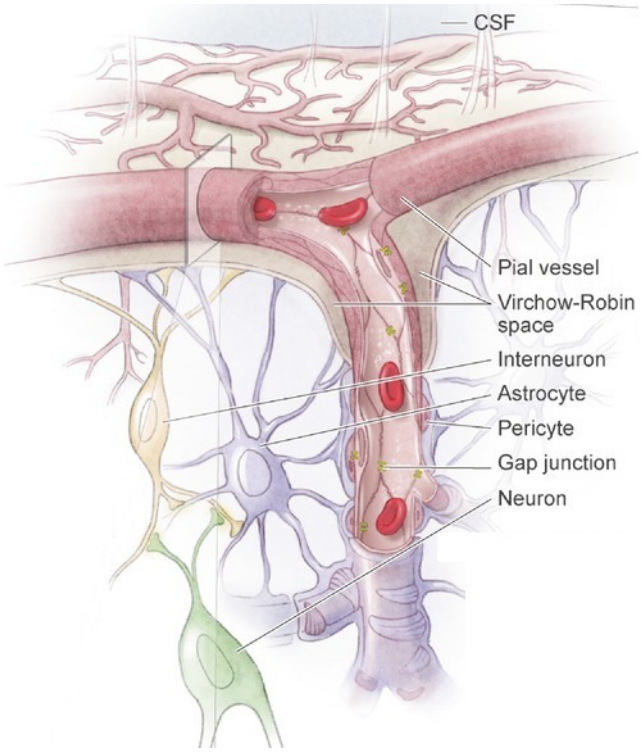

Figure 1.6: Neurovascular unit (Willie et al., 2014)

As shown in Fig 1.6, an arteriole is encapsulated by glial processes and pericytes, that release vasoactive substances, for which the arterioles respond mechanically by constricting or dilating according to changes in metabolic demand of the surrounding neural tissue.

The mechanisms outlined in this section are just a brief overview of major factors that affect cerebral blood flow regulation, the entire mechanism is of a much more complex nature and is not yet fully understood.

1.7 Aim and outline of thesis

Studies by Foreman and Claassen (2012) have shown that there are characteristic changes in EEG frequency in response to brain ischaemia, correlating with CBF and brain metabolism. Numerous clinical studies have also reported to show the change in EEG frequency with reducing CBF. Measurement techniques for both EEG and CBF are well developed, by which, ideally it would be possible to estimate

the blood flow regulation for e.g stroke patients in intensive care units and to provide treatment based on it. However the physiological understanding for interpreting this relationship currently does not exist. Modelling this relationship would enable us to vary the parameters over a wide range and provide better understanding of how to interpret the clinical measurements.

There are many haemodynamic models which attempt to explain the vascular dynamics in the brain. Using a haemodynamic model if there is a method to add a feedback loop between output (CBF) and the stimulus input (EEG/neuronal activity), the above relationship could be studied well. The desired model should be of closed loop, which consists a feedback loop from output (CBF) back to input. To the extent of our knowledge there currently exists no mathematical methods that could help in modelling this feedback. Hence, this study will focus on only the feed forward part of desired model.

In this study we thus attempt to vary the flow in a haemodynamic model by varying its flow resistance and simultaneously to vary input EEG frequency in order to simulate CBF. Then by using the known input variables and generated CBF, we perform autoregulation assessment to see how the input affects the autoregulation status. Specifically in this study we are interested in how changes in EEG input affects the assessment of autoregulation.

This thesis consists of six chapters, the first one introduces the background of cerebral circulation and autoregulation mechanisms. As our study requires EEG of various input, how the EEG signal is generated is detailed in the second chapter. In the third chapter the haemodynamic model used for this study is explained. In the fourth chapter the need of autoregulation assessment is briefed. Then the details of simulation parameters and simulations are discussed. In the fifth chapter, common methods for assessment of autoregulation are detailed. Then the assessment results are presented and discussed. Conclusions based on this study are provided in the sixth chapter.

Chapter 2

Neural Mass Model

2.1 Anatomy of Brain

The human nervous system is broadly divided into the peripheral nervous system (PNS) and the central nervous system (CNS). The PNS is the collection of spinal and cranial nerves whose branches spread to all parts of the body, conveying messages to and from the CNS. The CNS is composed of the brain and the spinal cord. The brain is composed of the cerebrum, the cerebellum and the brain stem.

Most of the CNS is divisible into grey matter and white matter. Grey matter contains a majority of dendrites and cell bodies. White matter contains a majority of axons. The area where grey matter forms a layered surface covering the cerebral hemispheres is referred to as the cortex. In each of the brain's two hemispheres the overlying cortex is divided into four anatomically distinct lobes: frontal, parietal, temporal, and occipital as shown in Fig 2.1. These lobes each have specialised functions.

The nervous system contains only two principal categories of cells - nerve cells, or neurons, and glial cells. Neurons convey information by a combination of electrical and chemical signalling mechanisms. All neurons have a cell body called soma, a series of branching and tapering processes called dendrites which receives information from other neurons via synaptic contacts (synapses), and one long, cylindrical part

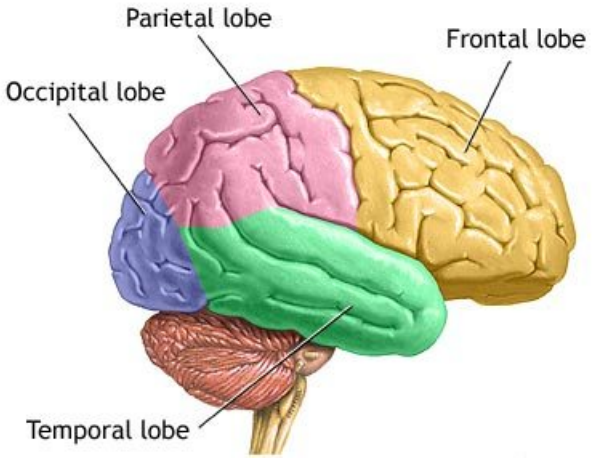

Figure 2.1: The major lobes of the cerebral cortex. (Source: www.nlm.nih.gov)

called an axon that conducts information away from the cell body. Hence neurons are anatomically and functionally polarized, with electrical signals travelling in only one direction. The electrical signals, called action potentials, are rapid, transient, all-or-none nerve impulses, with an amplitude of approximately 100mV and a duration of about 1ms. The nerve cell transmitting a signal is called the presynaptic cell. The cell receiving the signal is termed the postsynaptic cell. The schematic view of a typical neuron is shown in Fig 2.2.

2.2 Neural basis of *EEG*

2.2.1 Origins of *EEG*

The *EEG* (Electroencephalogram) is the recording of electrical activity of the brain which gives us the possibility of studying brain function with a high time resolution of the order of milliseconds. *EEG* signals reflect the summed electrical activity of populations of neurons. Neurons are excitable cells with characteristic intrinsic electrical properties, which, when stimulated, produce extracellular electric currents in the surrounding medium. Communication between neurons is mediated by electrochemical processes at synapses; consequently these cells produce electromagnetic fields that can be recorded at a distance from the source (da Silva, 2004). For these fields to

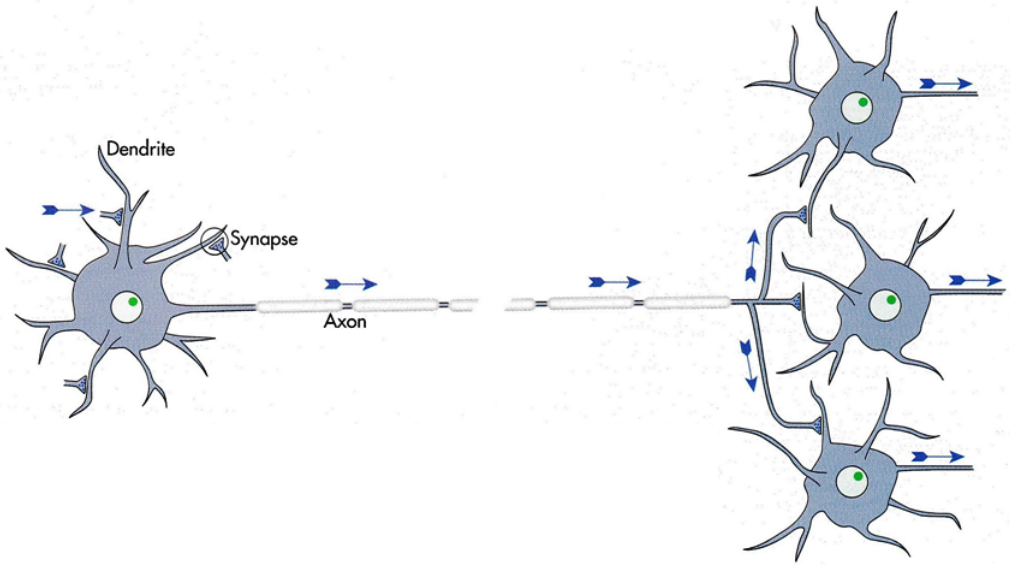

Figure 2.2: Typical view of neuron, indicating synaptic inputs to its dendrites and the arrows represents the information flow down the axon, reaching synaptic endings on other neurons (Nolte, 2008)

be measurable at a distance from the sources, it is important that the underlying neuronal activity is well organised both in space and time. The primary source for the generation of electromagnetic fields in a neural mass is the ionic current resulting from the changes in membrane conductance caused by synaptic actions. Primary trans-membrane currents are compensated for by secondary ionic currents flowing in along the intra- and extra-cellular spaces, since there can be no accumulation of electric charge. A portion of these secondary currents that flows through the extracellular space is directly responsible for the generation of field potentials.

The net membrane ionic current can be positive or negative, directed to the outside and inside of the neuron respectively. At the level of the synapse the inward current due to excitatory post-synaptic currents ($EPSC$) is positive, being negative in the case of inhibitory post-synaptic currents ($IPSC$). The current flow caused by $EPSC$ creates an active current sink; $IPSC$ creates an active current source in the extracellular region of the neuron thus forming a dipole configuration. Fig 2.3 shows the model of cortical pyramidal neuron showing current flow patterns caused by two modes of synaptic activation at an excitatory synapse at the level of the ap-

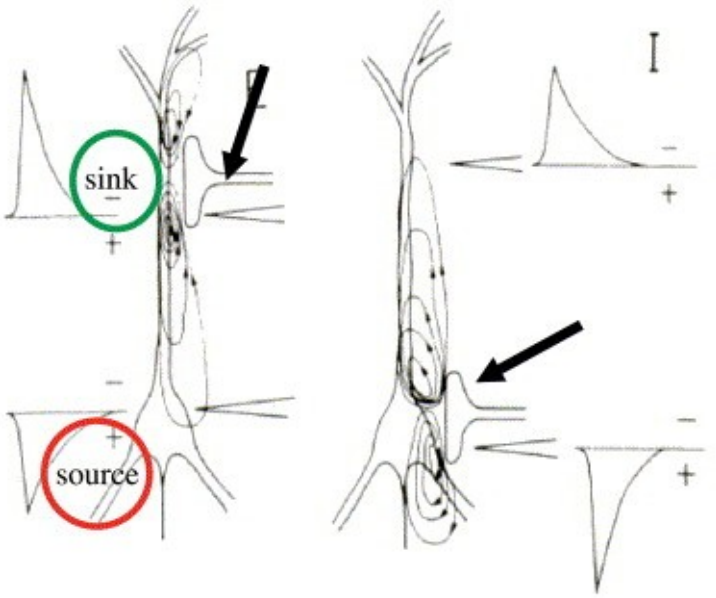

Figure 2.3: Model of cortical pyramidal neuron showing current flow patterns. (da Silva, 2004)

ical dendrite and an inhibitory synapse at the level of the soma. Depolarisation of the post-synaptic membrane causes excitatory postsynaptic potential ($EPSP$) in an excitatory synapse and an inhibitory postsynaptic potential ($IPSP$) in an inhibitory synapse. In Fig 2.3 (left), the flow of a net positive current creates a *current sink* in the extracellular medium next to the synapse. Shown top left is the extracellularly recorded $EPSP$, which has negative polarity at the level of the synapse. At the proximal part of the apical dendrite exists a distributed passive *current source* resulting in an extracellular potential of positive polarity. In Fig 2.3 (right), inhibitory synaptic activation creates an active *source* at the level of soma and a passive *sink* at the level of dendrites. In both cases a dipole source-sink configuration is created, and this is the generator of the electromagnetic field (da Silva, 2004). At the macroscopic level, to create a dipole layer, the mass of neurons should be spatially organised with dendrites aligned in parallel and synaptic activation must be synchronous. The pyramidal neurons of the cortex are aligned in parallel and their synaptic activation can occur within a cortical layer and in a synchronised way (da Silva, 2004).

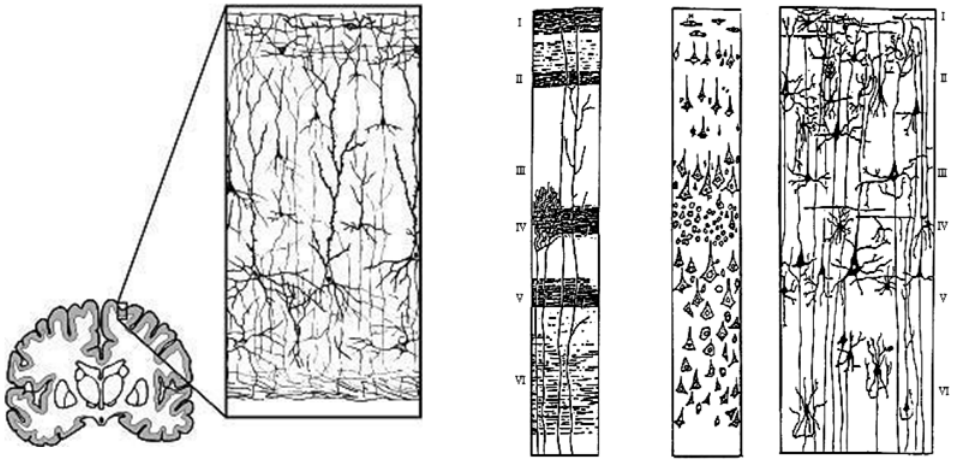

Figure 2.4: (Left)A cross section of the primate brain showing the folded cortical sheet (Mountcastle, 1957). (Right) Layered organisation of cortex (Nolte, 2008).

2.2.2 Cortex composition and organisation

The cortex is the superficial layer of the brain and represents the biggest part of the grey matter. It is organised in layers of different types of cells, shown in Fig 2.4. Most of the cortex is made up of six layers of neurons, layer I being at the cortical surface and layer VI lying next to the white matter with thickness varying from 3 mm to 6 mm (Jones and Peters, 2012). The neurons in the cortex can be divided into two classes: projection neurons and local inter-neurons. Projection neurons are excitatory with a pyramidal cell body and are situated in layers III, V and VI of the cortex. Inter-neurons amount for 20 to 25 % of neurons, are found in all layers and are often inhibitory. In the cortex, information processing is a multi-step process in which the axons of projection neurons carry information between stages and sometimes to distant group of neurons. In contrast inter-neurons receiving the same input as principal neurons convey it to local cells (Jones and Peters, 2012), (Kandel et al., 2000).

2.2.3 Cortical Columns

Cortical columns are formed by neurons stacked on top of each other through the depth of the cortex, which tend to be connected, and which respond to precise stim-

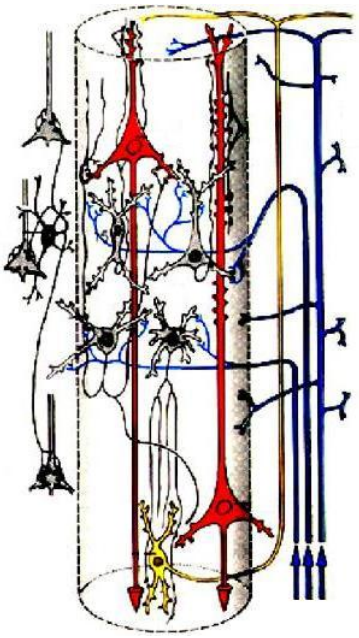

Figure 2.5: Depiction of a cortical column. The red coloured cells are Pyramidal neurons (Mountcastle, 1957).

ulations with similar activities throughout the layers. Cortical neurons spread their axons and dendrites from the cortex surface to the white matter forming a columnar organisation in the cortex, as shown in Fig 2.5. Experiments on somatosensory and visual cortices have made it possible to relate physiological cortical columns with sensory functions. (Mountcastle, 1957) showed that neurons inside columns of diameter 300 to 500μm displayed similar activities and called them *macrocolumns* which are commonly referred to as cortical columns. Hence to model the brain function one needs to model the cortical column.

2.3 Neural Mass Model

The generation of oscillations is complicated as there are many non linearities in the intrinsic membrane properties and the kinetics and interaction of inhibitory and excitatory neuronal populations (David and Friston, 2003). Modelling neural signals can be done in several ways, being either detailed models or reduced models. Detailed models include the complexity of individual neurons and synaptic connections: In such

models an individual neuron contains dendrites, soma, axon and several voltage-gated channel types. Then thousands of neurons and different types of interneurons are used to replicate the size of an actual biological network (Whittington et al., 2000). Reduced models consist of fewer neurons with simplifying assumptions about the neuronal activity. The neural mass model is based on the reduced model approach, comprising cortical columns with excitatory and inhibitory populations of neurons, using only one or two state variables to represent the mean activity of the whole population. We based our work on Jansen's model as it is the simplest model and as most of other neural mass models are based on this model.

2.3.1 Jansen's Neural Mass Model

Jansen's neural mass model (NMM) is based on the work of (Lopes da Silva et al., 1974) and (van Rotterdam et al., 1982). They developed a biologically inspired mathematical framework to simulate the spontaneous electrical activities of neuronal populations. In their model, populations of excitatory and inhibitory neurons were made to interact such that oscillations emerge, particularly oscillations in the α range of EEG (Jansen et al., 1993), (Jansen and Rit, 1995).

The model features a population of pyramidal neurons that receive excitatory and inhibitory feedback from inter-neurons in the same column and an excitatory input from neighbouring cortical columns and sub-cortical structures, such as the thalamus as shown in Fig 2.6.

The following physiological mechanisms of the cortex were taken into consideration in the model (Grimbert and Faugeras, 2006):

1. Existence of three neuronal populations (pyramidal cells, excitatory interneurons, inhibitory interneurons)
2. Feedback of information
3. Synaptic phenomena such as temporal dispersion, diffusion, and resistive-capacitive delay in the dendritic network

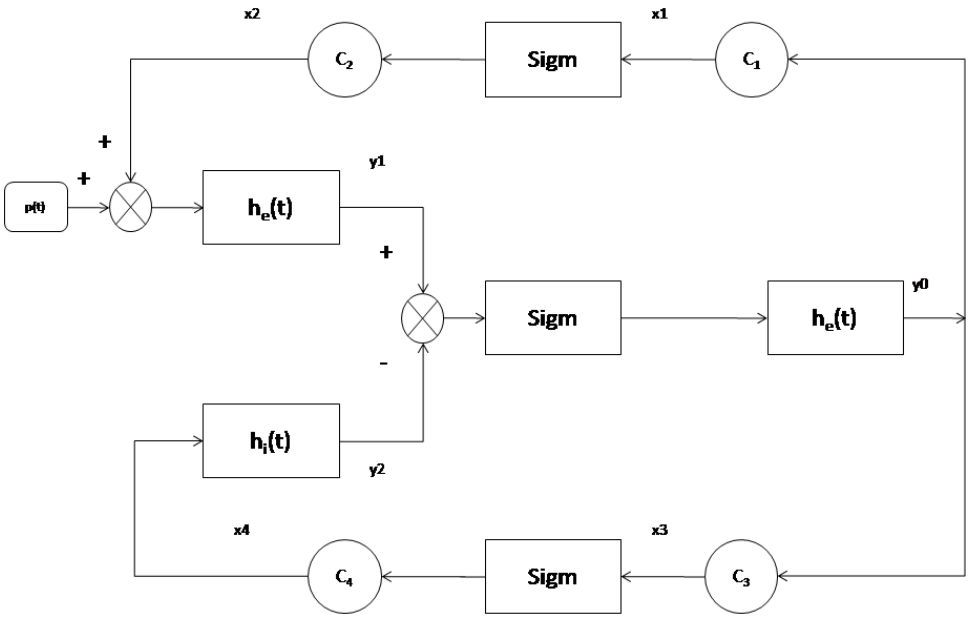

Figure 2.6: Jansen's Neural Mass Model of a cortical column

4. Interactions (linear and nonlinear) as observed in actual neuronal networks

The excitatory input is represented by an average firing rate $p(t)$. The input $p(t)$ can be noise accounting for background activity, an impulse function simulating a flash, signals from other columns or a combination of all of these. The three types of populations, pyramidal neurons, excitatory and inhibitory inter-neurons, and the synaptic interactions between populations are all modelled by different functions.

The first kind of block is called *post-synaptic* (h blocks, $h_e(t)$ or $h_i(t)$ where e represents excitatory populations and i inhibitory populations) which simulates synapses between the neuronal populations. They perform a second order differential linear transformation that converts the average firing rate of the presynaptic population into an average *post-synaptic* membrane potential. Its impulse response is given by:

$$h_e(t) = \begin{cases} Aate^{-at} & \text{t } \geq 0 \\ 0 & \text{t } < 0 \end{cases} \tag{2.1}$$

in the excitatory case and

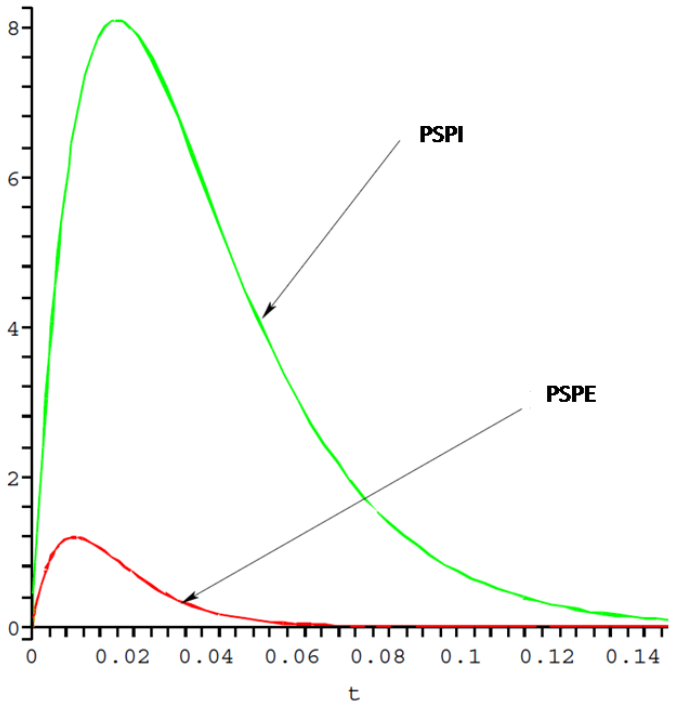

Figure 2.7: The post-synaptic potentials produced by the model. $PSPE$ - Excitatory postsynaptic potential, $PSPI$ - Inhibitory postsynaptic potential (Grimbert and Faugeras, 2006).

$$h_i(t) = \begin{cases} Bbte^{-bt} & \text{t } \geq 0 \\ 0 & \text{t } < 0 \end{cases} \tag{2.2}$$

in the inhibitory one.

The block accounting for synaptic transmission was designed by (van Rotterdam et al., 1982) to reproduce the shape and excitatory/inhibitory ratios of realistic post-synaptic potentials ($PSPs$) as shown in Fig 2.7. The synapses made by inhibitory neurons on the pyramidal neurons are closer to the cell body resulting in an effect about ten times stronger than that made by excitatory neurons.

The h blocks corresponds to solving a second order differential equation,

$$\ddot{y}(t) = Aax(t) - 2a\dot{y}(t) - a^2 y(t), \tag{2.3}$$

where $x(t)$ is the input to the $h_e(t)$ block and $y(t)$ the output. In the case of an

inhibitory block in the above equation A and a are replaced by B and b respectively.

Eqn 2.1 can also be written as a system of two first order differential equations

$$\begin{aligned} \dot{y}(t) &= z(t) \\ \dot{z}(t) &= Aax(t) - 2az(t) - a^2 y(t) \end{aligned} \tag{2.4}$$

A and B determines the maximum amplitude of the post-synaptic potentials. a and b are constants lumping together the membrane time constant and the different delays in the dendritic tree.

The other type of block in Jansen's model is the *Sigmoid* which introduces the nonlinearity in the model. The *Sigmoid* block simulates the soma of neurons by transforming the average membrane potential of the population into an output firing rate. It is described by the sigmoid function:

$$Sigm(v) = \frac{2e_0}{1 + e^{r(v_0 - v)}}, \tag{2.5}$$

where e_0 is half of the maximum firing rate of neuronal populations, v_0 is the value of the potential for which a 50% firing rate is achieved and r is the slope of the sigmoid at v_0.

The sigmoid transformation approximates the function that converts the membrane potential of a neuronal population into a firing rate as shown in Fig 2.8 . This sigmoid shape models the properties of neurons: if the potential is below an excitability threshold then no action potentials will be produced, around this threshold the firing rate increases linearly with the surface potential until it reaches a saturation value. Thus the sigmoid block could be considered to represent the average cell body action of a population. The other blocks C_1, to C_4 in the Jansen's model are the connectivity constants which account for the number of synapses between two populations.

Jansen's model can be completely described by writing equations similar to Eqn 2.3 for each post-synaptic output resulting in a set of six first order differential equa-

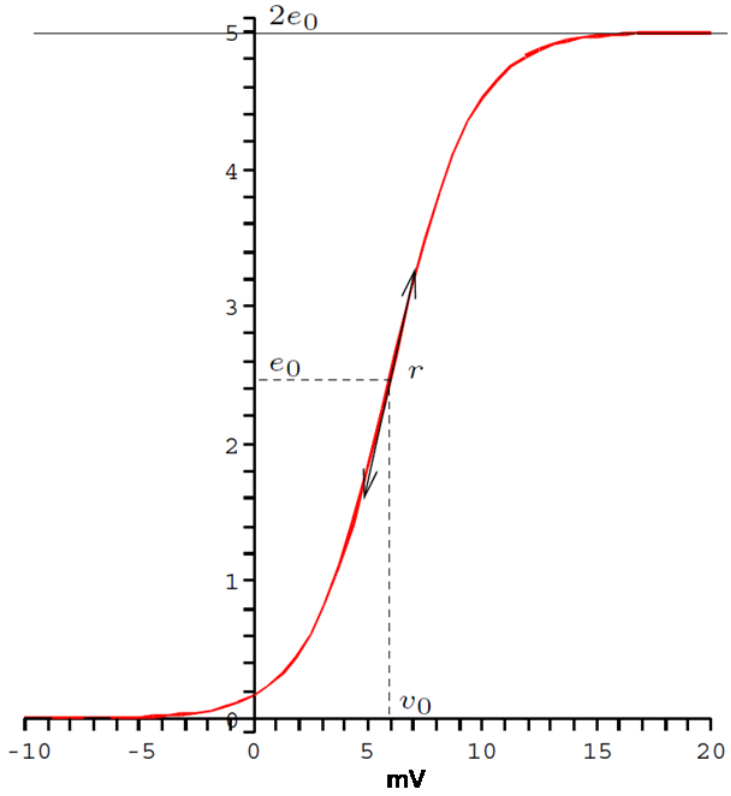

Figure 2.8: Sigmoid transformation performed by $Sigm$ 2.5

tions:

$$
\begin{aligned}
\dot{y_0}(t) &= y_3(t) \\
\dot{y_3}(t) &= AaSigm[y_1(t) - y_2(t)] - 2ay_3(t) - a^2y_0(t) \\
\dot{y_1}(t) &= y_4(t) \\
\dot{y_4}(t) &= Aa\left\{p(t) + C_2Sigm[C_1y_0(t)]\right\} - 2ay_4(t) - a^2y_1(t) \\
\dot{y_2}(t) &= y_5(t) \\
\dot{y_5}(t) &= BbC_4Sigm[C_3y_0(t)] - 2by_5(t) - b^2y_2(t)
\end{aligned}
\tag{2.6}
$$

The model's output is $y = y_1$-y_2, which is considered to be the output of the model because pyramidal neurons are the actual information transmitters from one column to another. Also the apical dendrites of pyramidal neurons reach to the superficial layers of the cortex where the potentials are summed and accounts for EEG activity (Kandel et al., 2000).

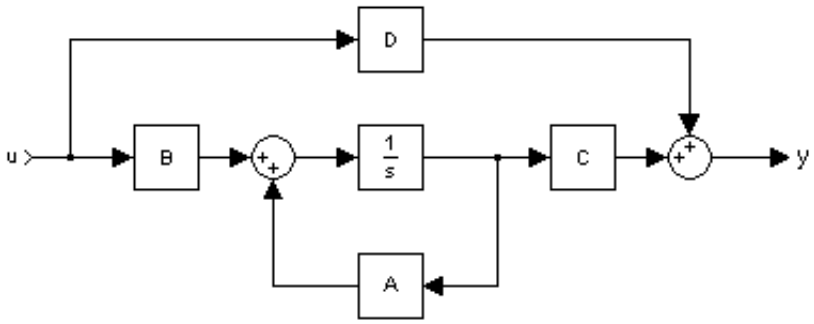

Figure 2.9: Typical State Space model

2.4 Generation of EEG

Jansen's neural mass model can be used to generate EEG signals. The model was implemented by the author using $MATLAB$ $Simulink$ by representing the set of differential equations describing the model in State Space form.

The mathematical model of a physical system is represented in State Space form with a set of input, output and state variables related by first order differential equations, based on the possibility that an n^{th} order differential equation can be written as n first order differential equations. A general continuous time-invariant State Space model in vector-matrix form is written as:

$$\begin{aligned} \dot{\mathbf{x}}(\mathbf{t}) &= A\mathbf{x}(\mathbf{t}) + B\mathbf{u}(\mathbf{t}) \\ \mathbf{y}(\mathbf{t}) &= C\mathbf{x}(\mathbf{t}) + D\mathbf{u}(\mathbf{t}) \end{aligned} \tag{2.7}$$

where $\mathbf{x}(.)$ is the state vector, $\mathbf{y}(.)$ is the output vector, $\mathbf{u}(.)$ is the input vector, A is the state matrix, B is the input matrix, C is the output matrix and D is the feedforward matrix.

Writing Eqn 2.4 in State Space form gives:

$$\begin{bmatrix} \dot{y}(t) \\ \dot{z}(t) \end{bmatrix} = \begin{bmatrix} 0 & 1 \\ -a^2 & -2a \end{bmatrix} \begin{bmatrix} y(t) \\ z(t) \end{bmatrix} + \begin{bmatrix} 0 \\ 1 \end{bmatrix} Aax(t) \tag{2.8}$$

2.4.1 Generation of EEG

EEG activity of different frequencies can be generated using Jansen's neural mass model which is described in State Space representation in the form of Eqn 2.8 as:

$$\begin{bmatrix} \dot{y_0}(t) \\ \dot{y_3}(t) \end{bmatrix} = \begin{bmatrix} 0 & 1 \\ -a^2 & -2a \end{bmatrix} \begin{bmatrix} y_0(t) \\ y_3(t) \end{bmatrix} + \begin{bmatrix} 0 \\ 1 \end{bmatrix} AaSigm\left[y_1(t) - y_2(t)\right], \tag{2.9}$$

$$\begin{bmatrix} \dot{y_1}(t) \\ \dot{y_4}(t) \end{bmatrix} = \begin{bmatrix} 0 & 1 \\ -a^2 & -2a \end{bmatrix} \begin{bmatrix} y_1(t) \\ y_2(t) \end{bmatrix} + \begin{bmatrix} 0 \\ 1 \end{bmatrix} Aa\left\{p(t) + C_2 Sigm\left[C_1 y_0(t)\right]\right\}, \tag{2.10}$$

$$\begin{bmatrix} \dot{y_2}(t) \\ \dot{y_5}(t) \end{bmatrix} = \begin{bmatrix} 0 & 1 \\ -b^2 & -2b \end{bmatrix} \begin{bmatrix} y_2(t) \\ y_5(t) \end{bmatrix} + \begin{bmatrix} 0 \\ 1 \end{bmatrix} BbC_4 Sigm\left[C_3 y_0(t)\right]. \tag{2.11}$$

The parameters $A = 3.25mV$, $B = 22mV$, $a = 100s^{-1}$ and $b = 50s^{-1}$ have been determined by (van Rotterdam et al., 1982) based on basic properties of real post-synaptic potentials for which the model will produce alpha activity. In Eqn 2.5 $v_0 = 6mV$ as suggested by (Freeman et al. (1975); Freeman (1987)), and and $e_0 = 2.5s^{-1}$, $r = 0.56mV^{-1}$ are the values used by (Jansen and Rit, 1995). The values for connectivity constants C_1 to C_4 are based on the neuroanatomical studies and have previously been estimated by counting synapses (Braitenberg and Schüz, 2013). Jansen and Rit (1995) related them all to a single parameter C: $C_1 = C, C_2 = 0.8C, C_3 = 0.25C, C_4 = 0.25C$. The input to the model $p(t)$ is a uniformly distributed noise ranging from 120 to 320 pulses per second corresponding to ongoing activity (background spontaneous activity) in the brain. The model was implemented in *Simulink* by the author and is shown in Fig 2.10. The implementation of the model was checked for correctness by comparing the output of our model with the results in

(Jansen and Rit, 1995).

2.4.2 Neural activity

The post-synaptic potentials and the action potentials are the main indicators for showing the activity in a neuron. Studies show that, due to there being more number of syapses per neuron in primates, post-synaptic responses are the dominant energy consumer accounting for 74% of energy (Attwell and Laughlin, 2001), action potentials consume 10% and rest of the energy is consumed by other processes. The output of the neural mass model is related to the synaptic activity of cortical column.

In Fig 2.10 each x_i represents the activation of several synapses firing with different time lag δ:

$$x_k(t) = h_k(t - \delta); \quad k = 1, 2, 3, 4 \tag{2.12}$$

where $h_k(.)$ is the same as in Eqn 2.1.

(Babajani and Soltanian-Zadeh, 2006), based on studies of (Logothetis, 2003) and (Attwell and Iadecola, 2002), proposed the following relation for neural activity in a cortical column:

$$N_k(t) \quad \alpha \quad I(h_k(t - \delta))(h_k(t - \delta)); \quad k = 1, 2, 3, 4 \tag{2.13}$$

where $I(h(t))$ is the current due to voltage $h(t)$ and the product $I(h(t))h(t)$ is a measure of the instantaneous power of the corresponding PSP. Considering a constant synaptic current:

$$N_k(t) \quad \alpha \quad (h_k(t - \delta); \quad k = 1, 2, 3, 4 \tag{2.14}$$

$N_k(t)$ gives the total power consumed. Neural activity N(t) is considered to represent the power consumed Eqns 2.12 and 2.14 is

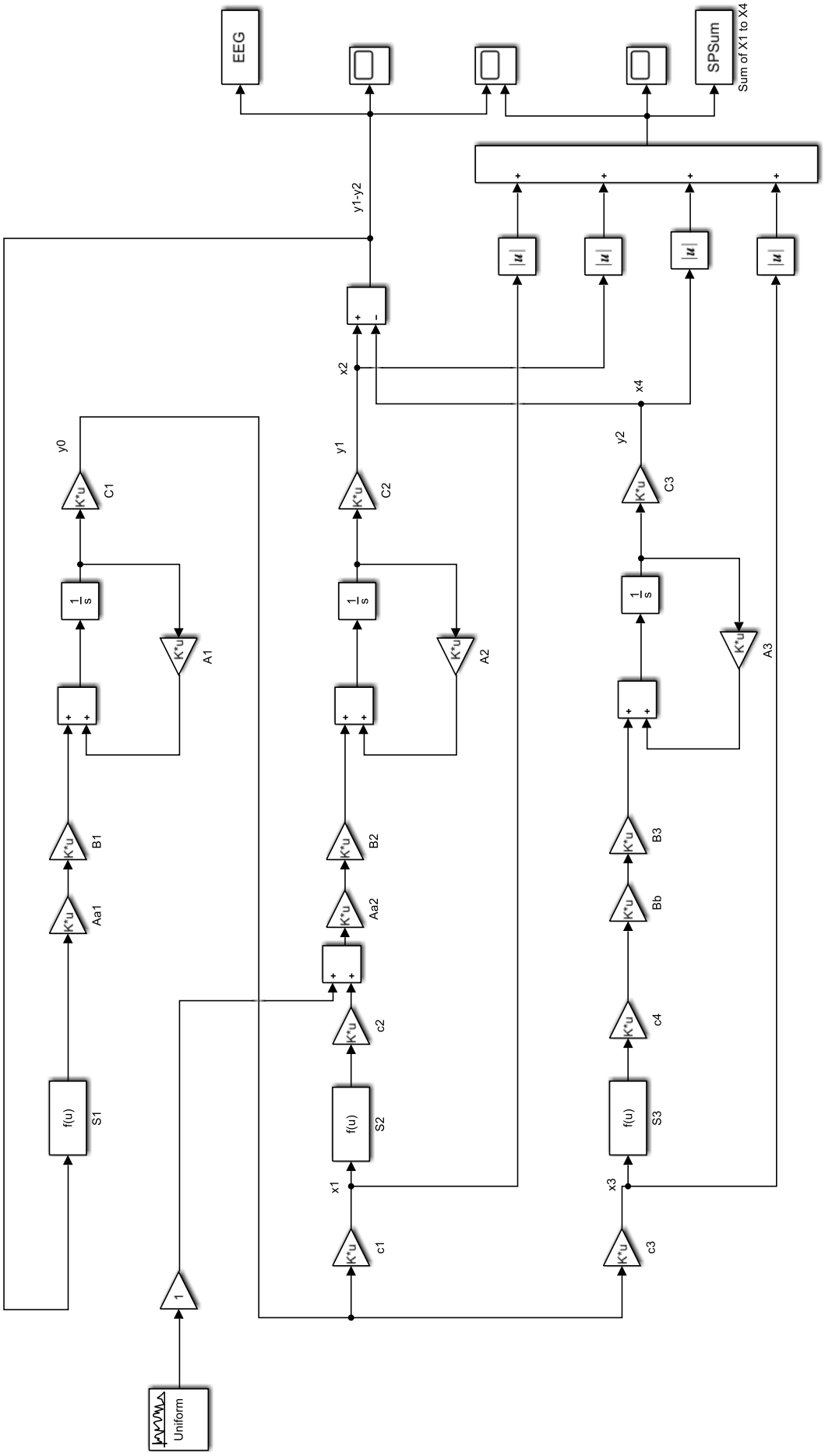

Figure 2.10: *Simulink* implementation of Neural Mass Model

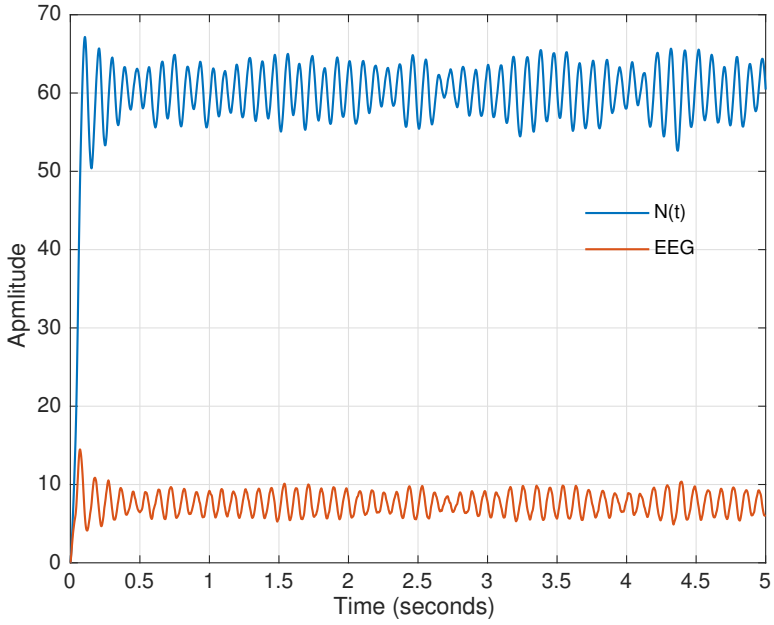

Figure 2.11: EEG and N(t) signals generated by Neural Mass Model

$$N(t) = \sum_{k=1}^{4} N_k(t) \quad \alpha \quad \sum_{k=1}^{4} x_k(t); \quad k = 1, 2, 3, 4 \tag{2.15}$$

The proportional gain ϵ called the "neuronal efficacy" is then introduced in Eqn 2.15 (Babajani and Soltanian-Zadeh, 2006).

$$N(t) = \epsilon \sum_{k=1}^{4} x_k(t); \quad k = 1, 2, 3, 4. \tag{2.16}$$

This is shown in Fig 2.10, where the absolute value of x1, to x4 are summed to get the neural activity (N(t)).

N(t) is the output of block SPSum in 2.10 and EEG is the output of block EEG. 2.11 show the plot of N(t) and EEG for 5 seconds duration. The signals N(t) and EEG are similar in nature except for amplitude difference. EEG signal is truncated for initial few seconds to discard the transients, then the DC component is removed and scaled, and the resulting signal is used as neural input u in model shown in 3.3.

2.5 Summary

The Jansen's neural mass model presented here is capable of generating EEG rhythms of various frequency. The model has a number of short comings as is the case with all mathematical models, as there are many assumptions made. However as the model parameters are related to architectural, neuro-chemical and behavioural characteristics of the cortical network, experimental verification of the model output might be possible, by comparing with actual EEG readings made under conditions where neuronal behaviour has been selectively altered (Jansen and Rit, 1995). In the context of this work this model serves well as it is a simplistic realisation of the highly complex neuro physiology and enables brain activity to be simulated realistically.

Chapter 3

Haemodynamic Model

3.1 Description of Haemodynamic Model

The haemodynamic model comprises of arterial, capillary and venous compartments. Very simply arteries regulates CBF, capillaries affect the gas transport and veins regulates CBV. The system of equivalence between hydrodynamic and electrical circuits is used in formulating equations as widely used by other authors, for example (Ursino and Lodi (1997); Ursino and Lodi (1998); Ursino et al. (2000)). The compartments of haemodynamic model are shown in Fig 3.1.

The arterial compartment is divided into two compartments, one regulating and the other non-regulating. The block R_{la} represents the larger part of the arteries down to, but excluding the large pial arteries. R_{sa} represents the smaller arteries and arterioles and is further divided into two blocks each of $R_{sa}/2$, with C_a between them to represent the changes in arterial volume. The division of the arterial compartment is based on the fact that active regulation takes place primarily in the smaller arteries and arterioles. Hence the non-regulating compartment has a fixed resistance (R_{la}) and fixed blood volume, whereas the regulating compartment has varying resistance (R_{sa}) and varying volume (C_a).

In the model capillaries are assumed to have fixed resistance and volume. The venous compartment is assumed to change in volume, represented by C_v, but to have

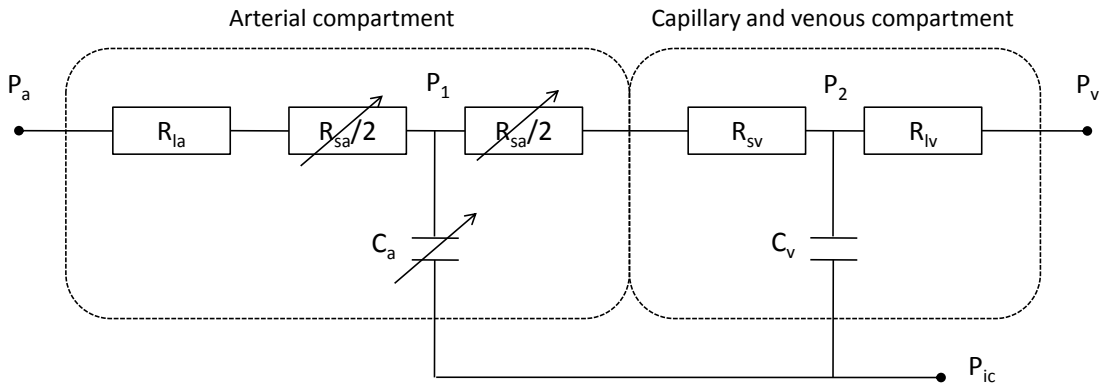

Figure 3.1: Schematic of haemodynamic model. P_a, systemic arterial pressure; R_{la}, resistance of non-regulating compartment; P_1, R_{sa}, and C_a, pressure, resistance, and compliance of regulating arterial compartment; R_{sv}, resistance of capillary compartment and small veins; C_v, venous compliance; P_2, venous pressure; P_v and R_{lv}, venous pressure and resistance of large veins, respectively; P_{ic}, intracranial pressure (Payne, 2006).

fixed resistance. Resistance due to smaller veins and capillaries is combined in one single resistance, represented by R_{sv}, R_{lv} representing the larger veins. Intracranial pressure (ICP) is assumed constant, since the time constants that govern ICP are significantly different from those of autoregulation (Giulioni and Ursino, 1996).

The arterial volume is assumed to comprise a fixed quantity, corresponding to the non-regulating vessels, V_{la}, and a varying quantity, corresponding to the regulating vessels, V_{sa}:

$$V_a = V_{la} + V_{sa}. \tag{3.1}$$

The resistance of a given vessel is proportional to the inverse of radius to the power four and volume of the vessel is proportional to the radius squared. For a given vessel length, its volume thus varies according to the inverse square root of resistance:

$$\frac{V_{sa}}{\overline{V_{sa}}} = \sqrt{\frac{\overline{R_{sa}}}{R_{sa}}}, \tag{3.2}$$

if it is assumed that regulating vessels constrict and dilate uniformly over their length.

The overbar is used to denote baseline conditions here and elsewhere.

From the definition of compliance, the rate of change of arterial volume can be related to the compliance and transmural pressure:

$$\frac{dV_{sa}}{dt} = \frac{d(C_a(P_1 - P_{ic}))}{dt}. \tag{3.3}$$

The key parameter in Eqn. 3.3 is arterial compliance, since it is assumed that CBF regulation occurs through changes in arterial compliance, i.e. change in the properties of the arterial vessel walls.

The equations for the change in venous volume are the same as in (Ursino et al., 2000), where venous volume is related to changes in transmural pressure:

$$\frac{dV_v}{dt} = C_v \frac{d}{dt}(P_2 - P_{ic}), \tag{3.4}$$

and venous compliance, C_v, is assumed to be inversely proportional to transmural pressure:

$$C_v = \frac{1}{k_{ven}(P_2 - P_{ic} - P_{v1})}, \tag{3.5}$$

where k_{ven} and P_{v1} are constants. Venous volume can then be directly calculated by substitution of Eqn. 3.5 into Eqn. 3.4 and integrating to give:

$$V_v = \left(\frac{1}{k_{ven}}\right) ln(P_2 - P_{ic} - P_{v1}) + V_{vn}. \tag{3.6}$$

The constant of integration, V_{vn}, is set to give a suitable baseline venous volume fraction.

The pressures in the haemodynamic model and arterial volume can be calculated from conservation of volume at the relevant nodes:

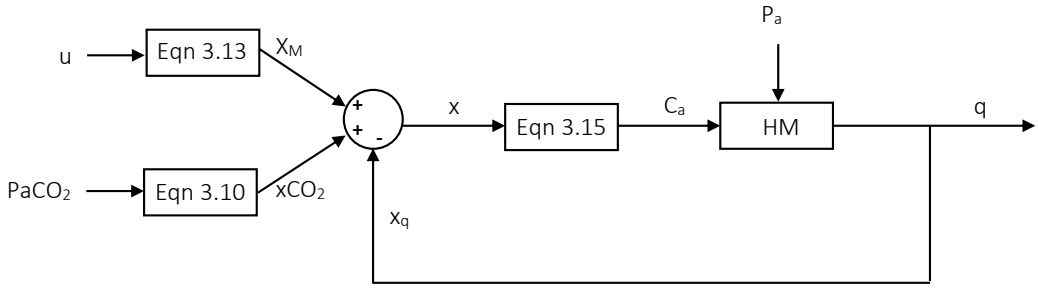

Figure 3.2: Schematic of feedback mechanisms. P_a, systemic arterial pressure; P_{aCO_2}, arterial partial pressure of CO_2; u, neural stimulus; C_a, compliance of regulating arterial compartment; q, cerebral blood flow; C_v, venous compliance; P_2, venous pressure; x_M, x_{CO_2} and x_q, state variables corresponding to feedback based on neural activity, CO_2 and cerebral blood flow, respectively. 'HD Model' refers to the haemodynamic model shown in Fig. 3.1 and numbers refer to equations.

$$\frac{dV_{sa}}{dt} = \frac{P_a - P_1}{R_{la} + R_{sa}/2} - \frac{P_1 - P_2}{R_{sa}/2 + R_{sv}}, \tag{3.7}$$

$$\frac{dV_v}{dt} = \frac{P_1 - P_2}{R_{sa}/2 + R_{sv}} - \frac{P_2 - P_v}{R_{lv}}. \tag{3.8}$$

The values of the parameters in the haemodynamic model are taken from (Payne, 2006), which are in turn adapted from (Ursino et al., 2000).

3.2 Feedback mechanisms

There are three potential mechanisms for adjusting compliance: CBF (autoregulation), arterial CO_2 concentration and neural stimulation. The way in which these mechanisms interact with each other and with the haemodynamic model is shown in Fig 3.2.

As in (Ursino et al., 2000), CBF and CO_2 regulation are assumed to be of the form:

$$\tau_q \frac{dxq}{dt} = -x_q + G_q \left(\frac{q - \overline{q}}{\overline{q}} \right), \tag{3.9}$$

$$\tau_{CO_2} \frac{dx_{CO_2}}{dt} = -x_{CO_2} + fn \left(\frac{P_{aCO_2}}{\overline{P_{aCO_2}}} \right). \tag{3.10}$$

In Eqns. 3.9 and 3.10, changes in CBF and arterial CO_2 (P_{aCO_2}) from their baseline values act to stimulate delayed changes in their respective state variables. The delays are mimicked by first order filters with time constants of τ_q and τ_{CO_2}, respectively. CBF regulation is assumed to act on the microvascular CBF:

$$q = \frac{P_1 - P_2}{R_{sa}/2 + R_{sv}}, \tag{3.11}$$

with a static relationship described by a constant gain G_q. For CO_2 the function in Eqn. 3.10 is selected to provide the best fit to the data as in (Reivich, 1964):

$$fn \left(\frac{P_{aCO_2}}{\overline{P_{aCO_2}}} \right) = 0.3 + 3 \tanh \left(\frac{P_{aCO_2}}{\overline{P_{aCO_2}}} \right) - 1.1). \tag{3.12}$$

The original model in (Ursino et al., 2000) was adapted by incorporation of a new state variable, x_M, which is assumed to be determined by the neuronal activity, u, using a second order dynamic model similar to that proposed by (Friston et al., 2000):

$$\tau_1^2 \ddot{x_M} + \tau_2 \dot{x_M} + x_M = \epsilon u, \tag{3.13}$$

where two time constants (τ_1, τ_2) govern the dynamic model (Payne, 2006). The scaling on the magnitude of the neuronal activity, ϵ, is taken to be one here. Observations by (Hoge et al., 1999) shows that the response to stimuli with increased concentrations of CO_2 is additive with the visually evoked stimulus. Following this the mechanisms are assumed to be linearly additive.

The three feedback mechanisms are assumed to act in a linearly additive manner:

$$x = x_M + x_{CO_2} - x_q. \tag{3.14}$$

Based on the combination of the three feedback mechanisms, changes in arterial compliance are modelled using an asymmetrical sigmoidal curve, as in (Ursino et al., 2000):

$$C_a = \overline{C_a} + \frac{1}{2}\left\{ \begin{array}{ll} \Delta C_a^+ \tanh\left(\frac{2x}{\Delta C_a^+}\right) & \text{x } >0 \\ \Delta C_a^- \tanh\left(\frac{2x}{\Delta C_a^-}\right) & \text{x } <0 \end{array} \right\} \tag{3.15}$$

The values of the parameters in the feedback mechanisms are all taken from (Payne, 2006). In this model compliance is thus directly dependent on a state variable, x, which is determined by the addition of the three inputs: ABP, CO_2, and u.

The haemodynamic model was implemented by the author using $MATLAB\ Simulink$ as shown in Fig 3.3 and simulation of Cerebral Blood Flow (CBF) was done with the model parameters as in Table 3.1.

3.3 Summary

In this chapter an unique haemodynamic model with simultaneous inputs for ABP, P_aCO_2 and neural stimulation was presented. Using this model CBF was generated for various input combinations. This model will be used in the following chapter to assess the effects of various inputs on the autoregulation capability of this model.

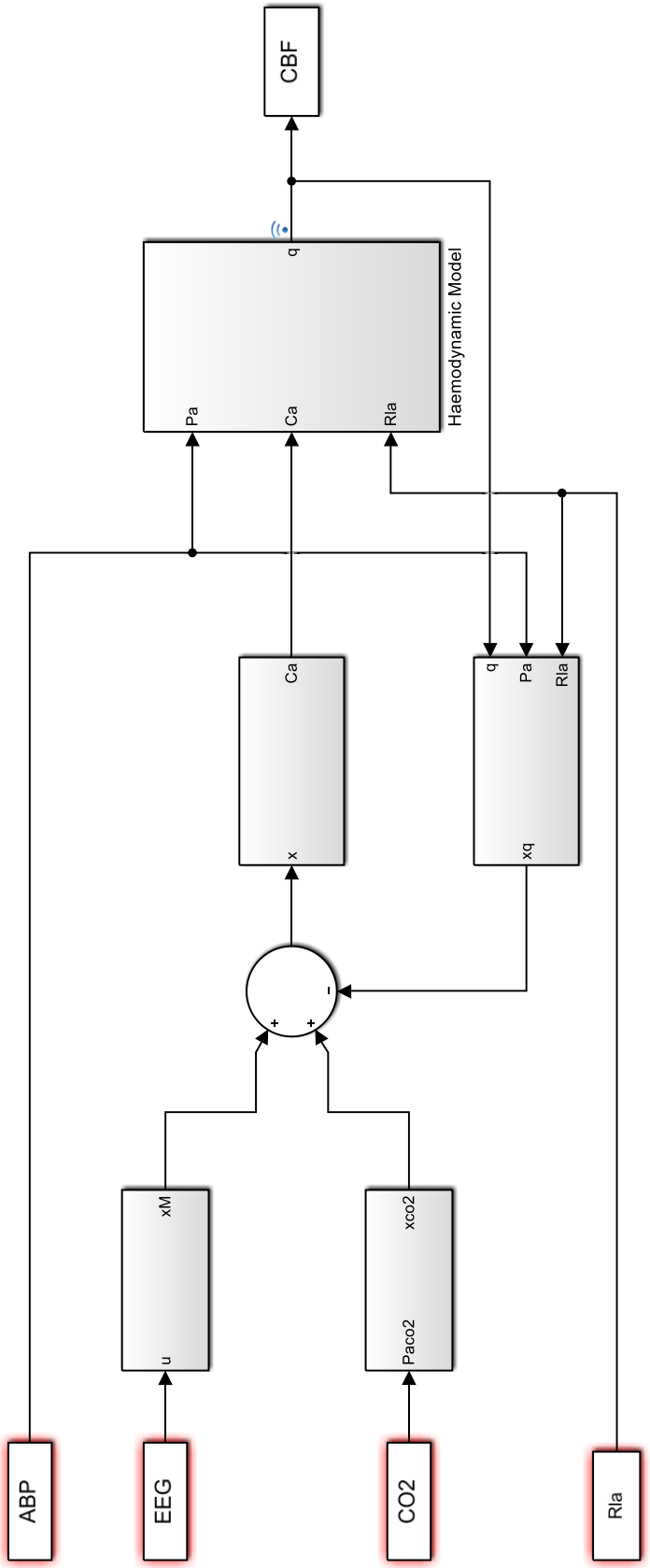

Figure 3.3: *Simulink* implementation of haemodynamic model

Parameter	Description	Value	
R_{la}	Resistance of large (non-regulating) arteries	0.4 mmHg s/ml	
R_{sa}	Baseline resistance of small (regulating) arteries	5.03 mmHg s/ml	
R_{sv}	Resistance of small veins (including capillaries)	1.32 mmHg s/ml	
R_{lv}	Resistance of large veins	0.56 mmHg s/ml	
P_a	Baseline arterial blood pressure	100 mmHg	
P_v	Venous outlet pressure	6 mmHg	
P_{ic}	Intracarnial pressure	10 mmHg	
P_{aCO_2}	Baseline arterial CO_2 pressure	40 mmHg	
P_{v1}	Pressure offset for venous compliance	-2.25 mmHg	
V_{la}	Volume of large (non-regulation) arteries	1 ml	
V_{sa}	Baseline volume of small (regulating) arteries	12 ml	
V_{vn}	Offset for venous volume	28 ml	
C_a	Baseline arterial compliance	0.205 ml/mmHg	
k_{ven}	Elastance coefficient for venous compliance	0.186/ml	
G_q	Gain of flow-based feedback mechanism	3.0 ml/mmHg	
τ_q	Time constant of flow-based feedback mechanism	20 s	
τ_q	Time constant of arterial CO_2 pressure	40 s	
τ_1	First time constant neural feedback	2 s	
τ_2	Second time constant neural feedback	4 s	
ΔC_a^+	Amplitude of positive change in arterial compliance	2.87 ml/mmHg	
ΔC_a^-	Amplitude of negative change in arterial compliance	0.164 ml/mmHg	

Table 3.1: Model parameters

Chapter 4

Combined model and experimental data

The Human brain needs a continuous supply of blood to provide for the needs of brain cells. As is the nature with blood supply to any other part of the body, interruptions in flow will lead to loss of function of cells, or cell death can occur. In the brain when the blood supply becomes restricted or is blocked, brain cells stops functioning normally and after certain time cells start to die. This leads to brain injury, termed stroke. There are two main categories of stroke, 1) ischaemic - caused when blood supply is stopped due to a clot in the blood vessels, this is the most common cause of stroke; 2) haemorrhagic - caused when blood vessel wall is weakened and the weak spot bulges and bursts, leading to reduced blood flow to upstream areas served by the vessel, and any a loss of blood out of the vessel pressurising brain cells and damaging those cells.

Ischaemia is caused by the blockage of blood vessels. It can be either embolic, where a moving mass of clot formed elsewhere moves in to narrow or block the upstream flow of blood, or thrombotic, where the obstruction arises at the spot of blockage, due to atherosclerosis.

During ischaemia, the area close to the blockage is called the core, where the blood flow is reduced to less than 20 percent of the normal flow. The area surrounding the

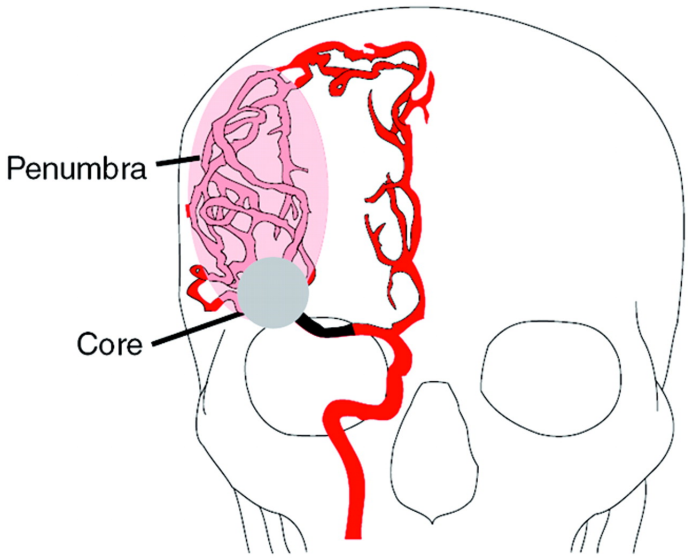

Figure 4.1: Ischaemia: Core and penumbra (Gonzalez, 2006)

core is called the penumbra, where blood flow is reduced but is still available supplied by the unblocked collateral arteries, to keep the neurons alive. In the core area, cells starts to die in 3 to 4 minutes, whereas in the penumbra area there is time, approximately 4-5 hours, available for medical intervention to restore the blood flow. This is shown in Fig 4.1.

The major share of energy expenditure, around 75% in brain is required for signalling processes, the remaining 25% being consumed by basic cellular activities (Hofmeijer and van Putten, 2012). The earliest consequence of ischaemia is disappearance of synaptic activity and failure of synaptic transmission has been proposed as the reason for electric silence in the penumbra (Hofmeijer and van Putten, 2012).

4.1 EEG changes in ischaemia

EEG changes correlate closely with changes in CBF (Sharbrough et al., 1973). When CBF is compromised, changes in metabolic and electrical activity of cortical neurons occur, which is reflected by changes in EEG (Foreman and Claassen, 2012). The change in EEG frequency in relation to reduction in CBF is shown in Fig 4.2.

With recent technical advancements, it is now possible to record and monitor

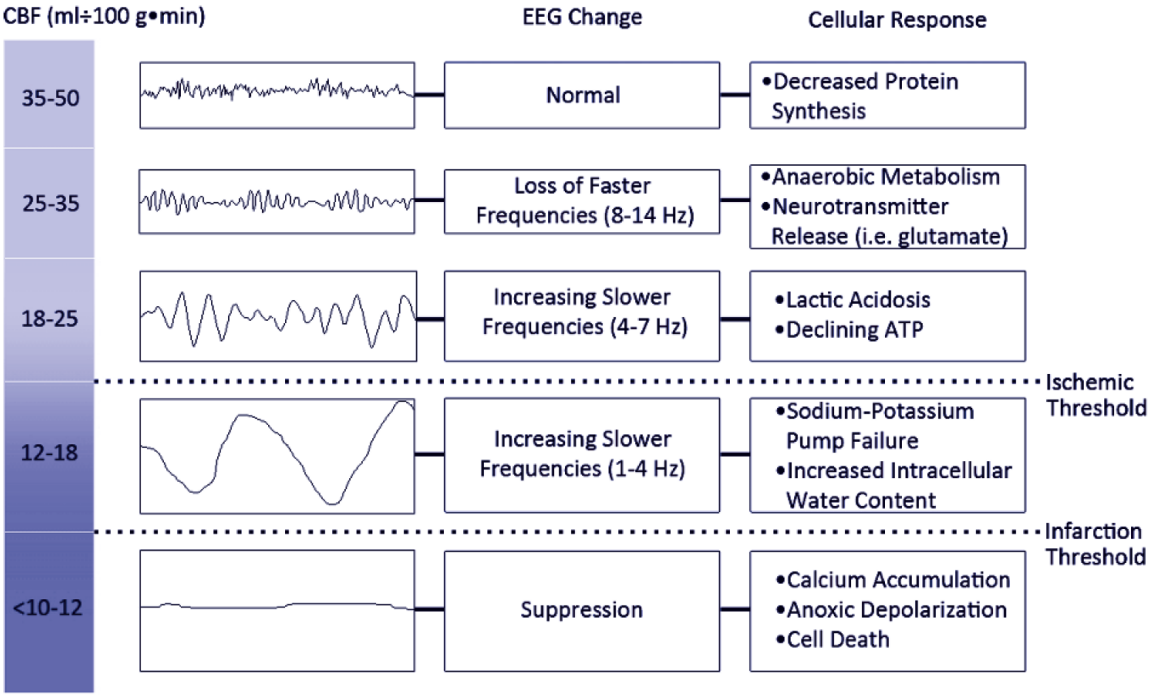

Figure 4.2: EEG and CBF (Foreman and Claassen, 2012)

continuous EEG (cEEG). cEEG provides instantaneous information about brain function which enables early detection of changes in neurological status in the clinical environment (Friedman et al., 2009). In cEEG subtle changes over time which span from hours to days may be missed even by trained expert, this has encouraged researchers to develop quantitative EEG (qEEG) (Foreman and Claassen, 2012). Still the interpretation of EEG signals remains quite challenging. There are a number of confounding factors, such as medication effects on EEG, and in ischaemic patients, removal of artefacts can be difficult (Payne, 2017).

4.2 Modelling the connection between EEG and CBF

As discussed in the previous section, the literature provides abundant information on how changes in EEG reflects the underlying changes in CBF. This provides an interesting case to mathematically model the connection between CBF and EEG.

This could be then incorporated in to the established haemodynamic model discussed in the previous chapter. But to the author's knowledge, there is no literature available which could provide the fundamentals required to establish a mathematical link between CBF and EEG.

Inspired by the link between CBF and EEG during ischaemia, we wish to investigate how EEG affects autoregulation using our haemodynamic model (HM). This is done by varying the model parameters to reduce the CBF in steps from its normal flow and then to evaluate the autoregulatory performance. This is assumed to be analogous to reducing levels of CBF during ischaemia.

4.3 Graded CBF and reducing EEG frequency

The CBF output of the HM can be varied by varying the value of R_{la}(resistance of non-regulating part of HM). CBF was reduced here from its normal baseline flow (100%) in 10% steps down up to 30%. The values of R_{la} corresponding to the reduced CBF were found by linearly varying R_{la} from its baseline value of 0.4, while the input u was kept at zero and other variables of HM were kept at their baseline values. R_{la} was chosen as it represents the larger arteries and is non regulating component in the model. This is shown in Fig 4.3.

Similarly EEG signals of different frequencies corresponding to change in CBF, as shown in Fig 4.2 were generated by changing the values of a, b and C in the NMM. David and Friston (2003), have shown in their study that by varying a, b and C they were able to generate EEG signals of varying frequency. They have provided the results for the range of a, b and C , but not specific values corresponding to specific generated signal frequency. Hence, the choice of a, b and C was made on trail and error basis by the author in order to generate signals of various frequencies.The signals generated by our model was compared to that shown in (David and Friston, 2003). The generated EEG signals are shown in Fig 4.4.

EEG of 25 Hz was assumed to be generated during the normal CBF of 100%, and

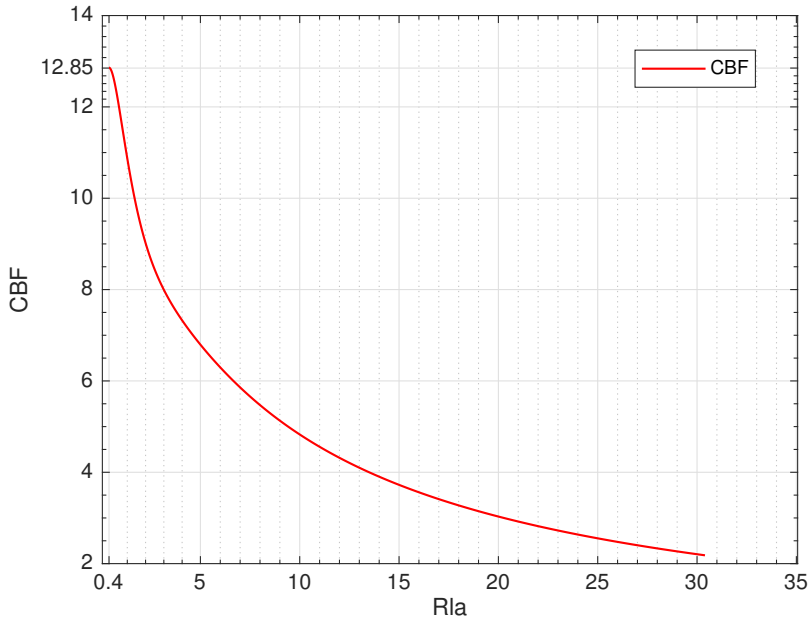

Figure 4.3: CBF values, as $R_{la}$is linearly increased from its initial value of 0.4

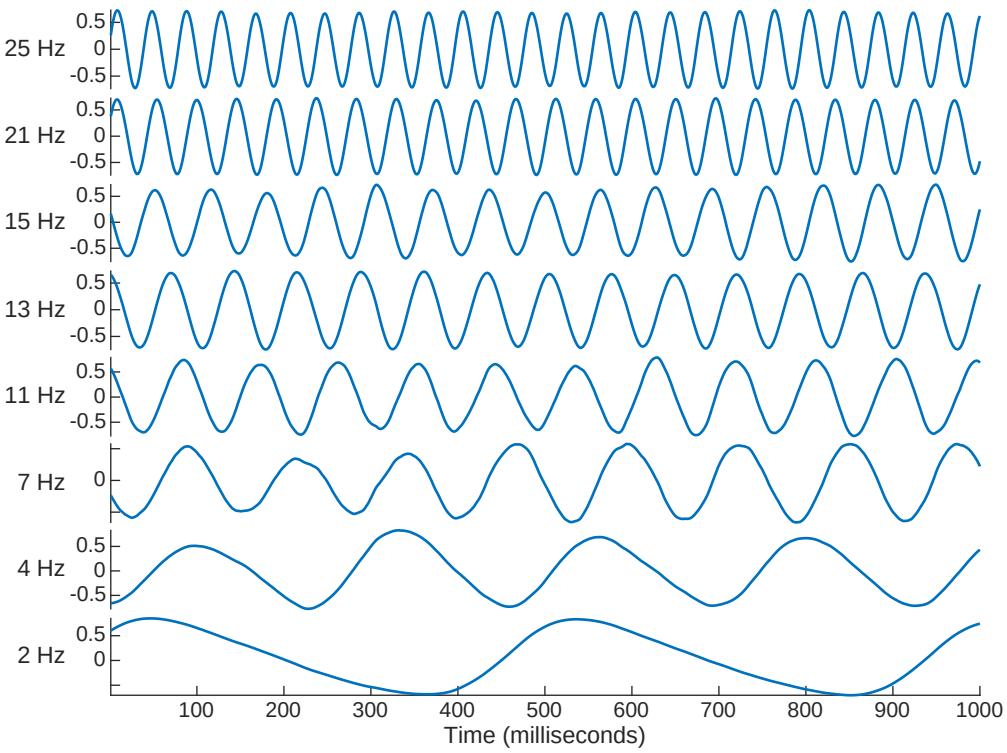

Figure 4.4: Generated EEG of various frequencies

CBF %	CBF (ml/100g/min)	Rla	a	b	C	EEG Frequency Hz
100	12.86	0.40	180	140	600	25
90	11.57	1.06	160	120	500	21
80	10.29	1.56	120	80	235	15
70	9.00	2.25	110	70	200	13
60	7.72	3.51	100	50	135	11
50	6.43	5.72	70	35	70	7
40	5.14	8.96	40	20	30	4
30	3.86	14.25	20	10	20	2

Table 4.1: Table of CBF, R_{la}, a, b and C values, generated together with EEG frequencies in Hz.

from there reducing EEG frequencies are assigned to reducing CBF percentages. The assignment of specific frequency to specific CBF level was completely arbitrary, the choice being made to reflect the results shown in 4.2. Table 4.1 shows the summary of reduced CBF and corresponding values of R_{la}, a, b and C, together with the assignment of generated EEG frequencies in Hz.

The reduction in CBF was done only up to 30%, as the relationship between R_{la} and CBF is non-linear, and any further reduction of CBF below 28.4% in our HM resulted in drastically high R_{la}which tended to cause simulation errors. Hence the lower limit of CBF was set to 30%.

4.4 Experimental data

In order to look into autoregulatory performance of our HM, simulations were performed with real subject data as inputs in the place of baseline values. The real subject data were the experimental data collected by Mitsis et al. 2004. The experimental data were obtained from fourteen subjects, all of them being healthy subjects. Data were collected under normal, free breathing conditions. None of the subject was on any medication and they were all normotensive. They all had no history of any

cardiovascular, pulmonary or cerebrovascular diseases. ABP was measured by finger photoplethysmography (Portapress, TPD Biomedical Instrumentation, Netherlands) and CBF velocity ($CBFV$) was measured by transcranial Doppler ultrasonography in the right middle cerebral artery(TC22, SciMed, Briston, U.K.). With CBFV signal measured, assuming there is no change in vessel diameter, the same signal can be considered as a measurement of CBF. This has been found to represent the signal well in almost all practical cases, as detailed in Mitsis et al. 2004, and (Poulin and Robbins, 1996). Partial pressure of end-tidal CO_2($P_{ET}CO_2$) was measured by mass spectrometry (AMIS2000, Innovision, Odense, Denmark). In a healthy person breathing air normally the difference between $P_{ET}CO_2$ and P_aCO_2 is small, with $P_{ET}CO_2$ being lower than $P_aCO_2$by 2-5 mmHg. The reduction in value, in a healthy person is due to anatomical dead space, where other exhaled gases mixes with the alveolar CO_2. When there is alveolar dead space due to some pathology the difference increases (McSwain et al. 2010, Huttmann et al. 2014). $P_{ET}CO_2$ can be used as a surrogate for P_aCO_2(McSwain et al., 2010). In this study the experimental data for $P_{ET}CO_2$ were obtained from healthy subjects and will be used as the input for P_aCO_2 in our model shown as in Fig 3.2. The experimental data values of $P_{ET}CO_2$ is given in Table 4.2. The mean values tend to vary considerably from a minimum of 28.85 mmHg to a maximum of 40.42 mmHg. Hence it will be assumed that the difference between end-tidal and arterial measurements will not be significant. Further as the results are interpreted based on the mean value of all subject data, this difference will not impact the observation of results. In all the following text the experimental data is referred to as values for P_aCO_2.

All experimental signals were sampled every 10 ms. Real time beat-to-beat values of mean ABP ($MABP$) and mean $CBFV$ ($MCBFV$) were calculated by integrating the sampled signals over each cardiac cycle (RR interval). Resulting signals were then interpolated and re-sampled at 1 Hz to obtain equally spaced time series of $MABP$ and $MCBFV$, similarly breath-to-breath data were interpolated to obtain values

Subject	ABP (mmHg)		$P_{ET}CO2$ (mmHg)	
	Mean	SD	Mean	SD
1	79.62	2.48	40.42	0.66
2	67.46	5.03	40.39	1.31
3	72.88	3.24	39.50	1.07
4	74.38	2.77	38.86	0.75
5	75.51	3.68	35.99	0.73
6	85.70	4.01	36.60	0.69
7	78.98	3.38	37.65	1.13
8	67.86	3.37	37.27	0.93
9	64.49	4.08	36.53	1.32
10	83.37	3.99	36.40	1.06
11	85.87	3.80	35.60	0.66
12	81.42	5.11	35.91	0.44
13	78.65	3.08	35.35	0.82
14	78.63	3.57	28.85	0.68
	76.77	3.685	36.80	0.87

Table 4.2: Mean and SD of ABP and $P_{ET}CO_2$ for 14 subjects

spaced at 1 sec (Mitsis et al., 2004). The length of the time series signals was 2000 seconds. Table 4.2 shows the mean and standard deviation of the values of ABP and $P_{ET}CO_2$ for all the 14 subjects .

A short segment (200 seconds) of signals ABP, $CO2$ and CBF from the experimental data of subject 4, is shown in Fig 4.5. Also shown in the figure is the generated CBF corresponding to the input signals.

4.5 Generating CBF

To study the effects of varying ABP, P_aCO_2 and stimulus input (EEG) on the CBF, real subject data were used as inputs to respective variables in our HM. This would give us generated CBF, which could be compared with experimental CBF. Various analysis methods, discussed later, will then give insights in to effects of these variables

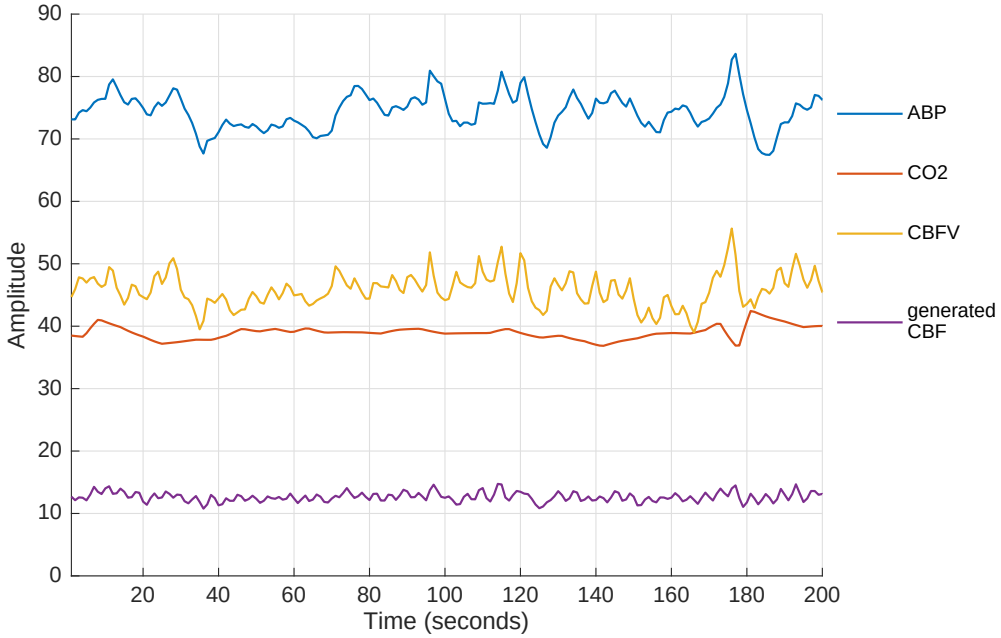

Figure 4.5: Segment (200 seconds) of experimental data for subject 4

	Colour	ABP	P_aCO_2	EEG (input)
Case 1		Data	40	Nil
Case 2		Data	Data	Nil
Case 3		Data	40	Yes
Case 4		Data	Data	Yes

Table 4.3: Combination of variables for Simulations

on the CBF output. We intend to study the effects of three variables on the CBF output using our HM. Those three variables are ABP, P_aCO_2 and stimulus input (EEG). To study the effects of real ABP, simulations were carried out by only varying ABP and keeping P_aCO_2 at a baseline value and the EEG input as zero.

Next, to study the effect of changes in P_aCO_2, real data for P_aCO_2 were used while the input EEG was kept at zero. Then to study the effect of input EEG, while using real data for ABP and P_aCO_2, the simulated EEG was used. This is illustrated by colour coding each case as shown in Table 4.3. This colour coding represents the combination of inputs used to generate CBF, and in the rest of this thesis.

To simulate the reduction of blood flow during ischaemia, CBF values were de-

	CBF Levels in %							
	100	90	80	70	60	50	40	30
	*	*	*	*	*	*	*	*
	*	*	*	*	*	*	*	*
	*	*	*	*	*	*	*	*
	*	*	*	*	*	*	*	*

Table 4.4: Illustration of simulations for various percentages of CBF

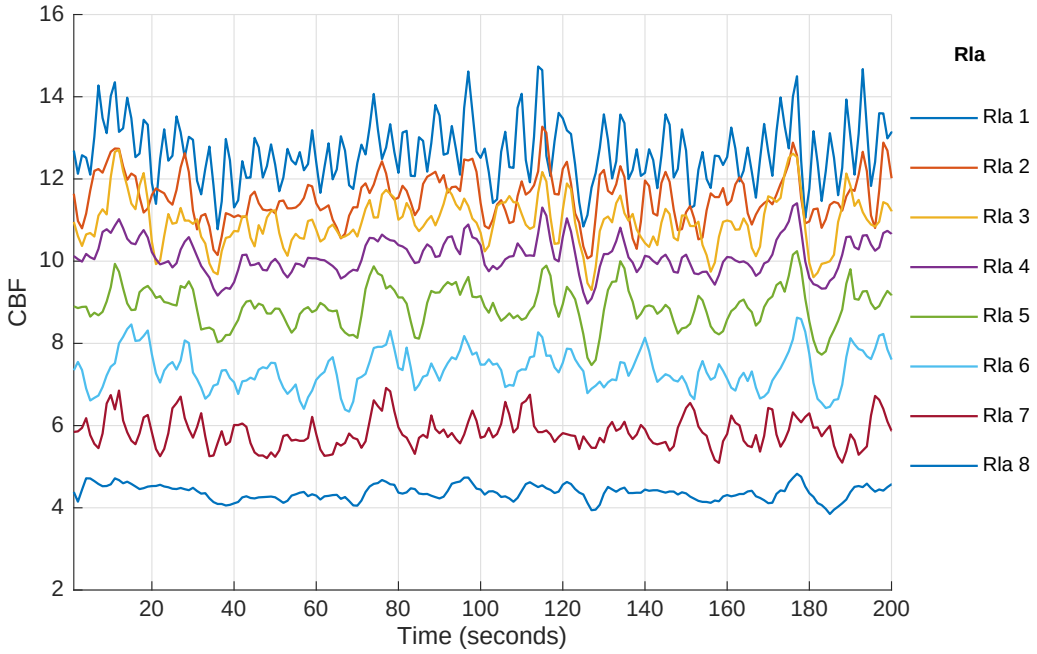

Figure 4.6: Generated CBF for eight R_{la} values

creased in 10% intervals. Next, to study the effects of changes in ABP and P_aCO_2 during the reduced levels, the simulations mentioned in the previous paragraph were repeated for all the reduced levels of CBF. This is illustrated in Table 4.4.

The above table of simulations were carried for all 14 subjects. The length of experimental data used for all simulations was 2000 seconds. When simulations were carried out as discussed above, it resulted in a 3D matrix of generated CBF signal of size 4 (cases) X 8 (CBF levels) X 14 (subjects). This 3D matrix of generated data was then used for autoregulation assessment analysis.

Fig 4.6 shows a segment (200 seconds) of generated CBF for eight R_{la} levels (Table 4.1), for case 4 (Table 4.3), with input being the signals from subject 4. It

clearly shows the reduced values of CBF for reducing R_{la} values.

4.6 Summary

In this chapter the need for assessment of autoregulation was discussed. The methods used to simulate the changes in EEG frequency for reducing levels of CBF using the neural mass model and the haemodynamic model are detailed. The parameters used in these models were presented. Experimentally collected data of fourteen subject's ABP and P_aCO_2 were given in this chapter. Finally how simulated CBF data were generated was discussed and various cases for combinations of input detailed.

Chapter 5

Autoregulation Assessment Results

5.1 Introduction

CBF under normal physiological conditions is matched to the metabolic demands of brain (Jordan and Powers, 2012). This is accomplished by several structural as well as adaptive features of the cerebral circulation. The main adaptive feature is cerebral autoregulation which is a complex multi-factorial process. In both animal and human studies it has been demonstrated clearly that CBF remains relatively constant within a fixed range even when there are significant fluctuations in $MABP$ (Jordan and Powers, 2012).

In humans who are normotensive the range of autoregulation where CBF remains relatively constant is between 60 - 150 mmHg. Whenever the $MABP$ changes beyond this limits of autoregulation CBF becomes unregulated and there is a risk of brain injury. Below a critical threshold of CBF ischaemia occurs and can lead to irreversible loss of brain tissue, and beyond the upper limit the loss of autoregulation results in endothelial injury and breakdown of the blood brain barrier resulting in cerebral oedema. The integrity of cerebral autoregulation is of significant clinical importance (Jordan and Powers, 2012).

5.2 Assessment of Autoregulation

To make an assessment of autoregulation, the crucial parameter required to be accurately measured is the CBF (Payne, 2016). Autoregulation is defined by the relationship between ABP and CBF, and measurements of both parameters are now relatively easy (Payne, 2017). There have been very many studies that have attempted to quantify this relationship, falling under two categories, static and dynamic autoregulation methods.

Static autoregulation is assessed by analysing changes in CBF in response to a change in ABP over a timescale of minutes (to hours) and it reflects a steady-state response (Klein et al., 2019). Static autoregulation often requires the use of pharmacological agents to induce steady-state changes in blood pressure (Sanders et al., 2019).

Dynamic autoregulation analyses changes in CBF in response to spontaneous or generated fluctuations using computational techniques. This could include linear or nonlinear methods, using either time or frequency domain analysis, to evaluate the relationship between ABP and CBF (Klein et al., 2019).

5.3 Transfer function analysis

Among various methods that have been proposed for the investigation of autoregulation, one popular method is transfer function analysis (TFA) (Liu et al., 2015). TFA quantifies autoregulation in terms of parameters of gain, phase and coherence (Claassen et al., 2016). The TFA method is based on the assumption that autoregulation can be modelled as a linear high pass filter which allows fast changes in ABP to pass to CBF while attenuating low frequency oscillations (Liu et al., 2015). Autoregulation functions like a high pass filter, allowing fast changes in ABP to pass through while slow changes in ABP are filtered. Therefore the relation between ABP and CBF can be expressed by TFA using a high pass filter model in the frequency

range of 0.07 to 0.30 Hz (Van Beek et al., 2008).

The TFA method is characterised by three parameters, gain, phase shift and coherence. The gain quantifies the amplitude change between the input and output of TFA. A low gain indicates an intact autoregulation, whereas an increase in gain represents impaired autoregulation.

The next parameter in TFA, phase shift, describes the inertia of the filter, which is seen as a shift (delay) in the phase value between the input (ABP) and output signal (CBF). This is due to the fact that changes in CBF recover faster than the changes in ABP which causes the displacement of the CBF signal in relation to the ABP signal. When the CBF signal leads (phase lead) in respect to the ABP signal, autoregulation is interpreted to be intact, whereas a phase shift closer to 0 indicate a complete loss of autoregulation (Van Beek et al., 2008).

The third parameter in TFA is the coherence function which reflects the linear correlation between the input and output at a given frequency. A coherence value close to 1 in a specific frequency range suggests that the input and output signal are linearly related (Liu et al., 2015).The coherence value will be reduced when there is a significant degree of nonlinearity between the signals. Fig 5.1 shows the overview of transfer function analysis method.

Software created by CARNET group was used for TFA method of autoregulation assessment (Simpson, 2015). The inputs are ABP and $CBFV$, and the parameters used were the default parameter settings as detailed in (Claassen et al., 2016).

5.4 Autoregulation Index (ARI)

The Autoregulation Index (ARI) is a metric to quantify cerebral autoregulation, first proposed by Tiecks et al. (1995). ARI has become one of the most commonly used methods to assess autoregulation. In this method a second order linear model defined by a set of three difference equations is used to attain an output (CBFV response) for a given input (ABP). Then the resulting estimated CBFV signal is compared

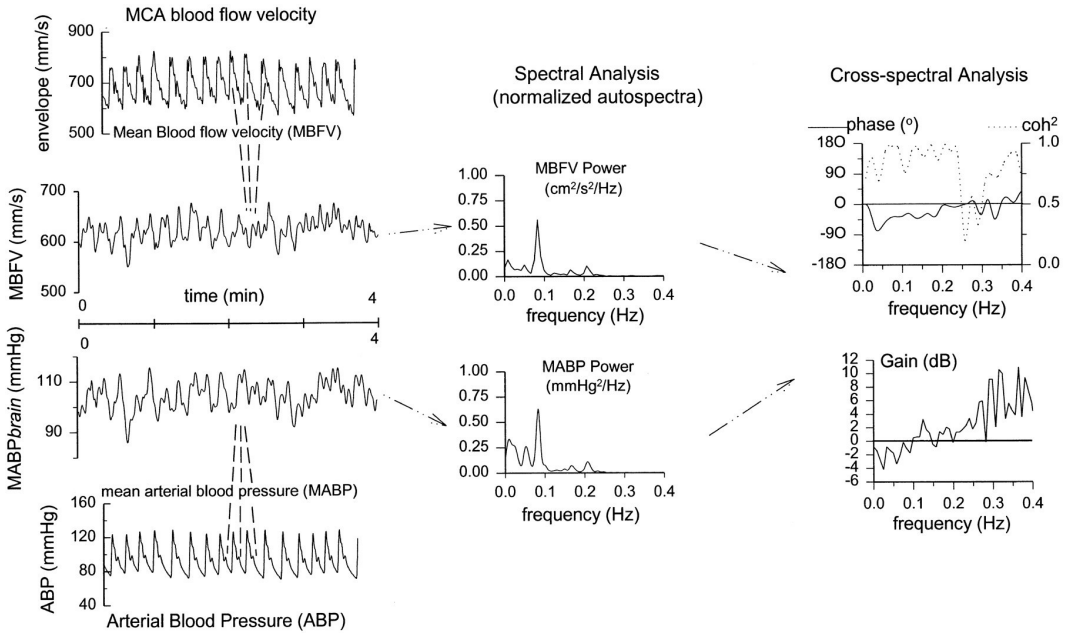

Figure 5.1: Illustration of Transfer Function Analysis (TFA) method (Blaber et al., 1997)

with 10 template CBFV signals produced for 10 set of values of parameters in the second order model. The comparison is given an index value in the range of 0 to 9. An ARI of 9 is considered maximal autoregulation and ARI of 0 is considered as a total absence of autoregulation.

5.4.1 ARI Model

The Tiecks method for finding ARI is described here (Tiecks et al., 1995). ABP and CBFV timeseries are denoted by $P[t]$ and $V[t]$ respectively, of length N and indexed by t. Let P_m and V_m denote the mean value of $P[t]$ and $V[t]$ for the entire interval of interest.

The time varying ABP signal $P[t]$ is normalised as follows

$$dP[t] = \frac{P[t] - P_m}{P_m - P_{cr}} \tag{5.1}$$

where $P_{cr} = 12mmHg$ is the critical closing pressure.

The following system of difference equations is used to compute the intermediate

variables x_1, $x_2$as

$$x_1[t] = x_1[t-1] + \frac{dP[t-1] - x_2[t-1]}{fT} \tag{5.2}$$

$$x_2[t] = x_2[t-1] + \frac{x_1[t-1] - 2Dx_2[t-1]}{fT} \tag{5.3}$$

where f is sampling frequency, D is damping factor and T is time constant.

The modelled CBFV, denoted by $\hat{V}[t]$, is computed as

$$\hat{V}[t] = V_m \left(1 + dP[t] - Kx_2[t]\right)$$

where K is a parameter representing autoregulatory gain.

In order to start the process at steady-state the initial conditions for the intermediate variables are selected as

$$x_1\left(0\right) = 2DdP[0], \quad x_2\left(0\right) = dP[0] \tag{5.4}$$

Tiecks et al. (1995) have used 10 sets of values for model parameters T, D and K, as given in Table 5.1. Each set of values for these parameters results in a reference curve, corresponding to autoregulation ranging from 0 (absence of autoregulation) to 9 (strongest autoregulation).

The step response of Tiecks et al. (1995) model for a step change in ABP is shown in Fig 5.2.

Let $\hat{V}_j[t]$, where $j = 0, 1, ...8, 9$, denote the response of the model for the j^{th}set of the parameters (T, D, K).

The ARI is determined by first finding the Euclidean norm of $\frac{\hat{V}_j[t] - \hat{V}[t]}{V_m}$, for each of the j^{th} response, which gives us an array of 10 values. Then this array is interpolated by cubic splines to create a smooth curve so that fractional values of ARI can be determined. The minimum value of the interpolated curve is the ARI value.

ARI	T	D	K
0	2	0	0
1	2	1.6	0.2
2	2	1.5	0.4
3	2	1.15	0.6
4	2	0.9	0.8
5	1.9	0.75	0.9
6	1.6	0.65	0.94
7	1.2	0.55	0.96
8	0.87	0.52	0.97
9	0.65	0.5	0.98

Table 5.1: Sets of values for the parameters T, D and K which produces ten reference curve

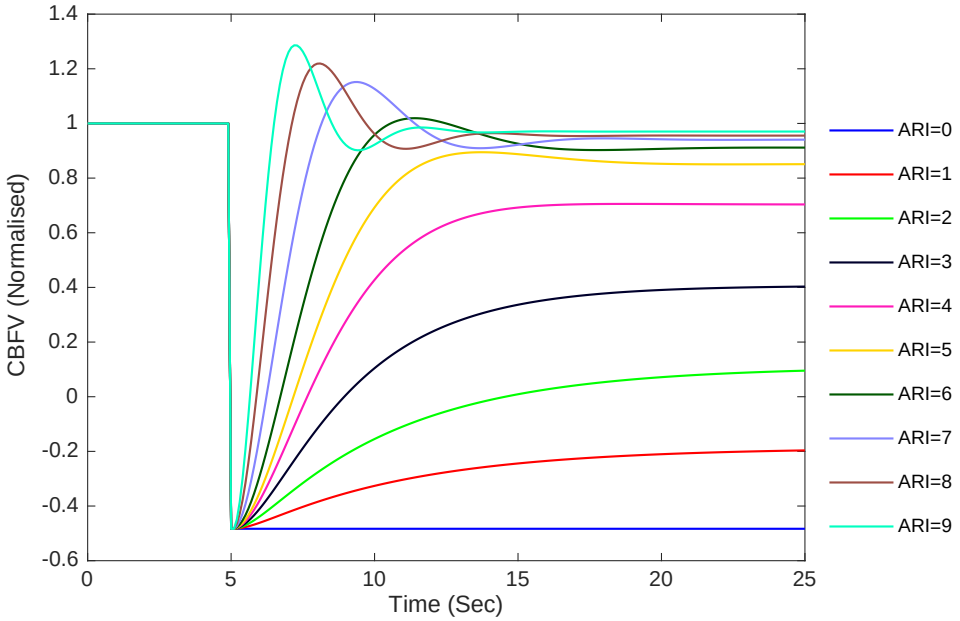

Figure 5.2: Step response of Tiecks et al. (1995) model for a step drop in ABP

5.5 Simulations

Simulation are performed by feeding the inputs to the HM and the output is then the generated CBF. The generated CBF is analysed by the two autoregulation assessment methods described earlier, the TFA method and ARI method. CBF is used as a surrogate for CBFV while using the assessment methods, since both the methods look for the spontaneous variations in the signals and this is valid when the vessel cross section area is assumed to be constant.

Our HM was modelled for the baseline value of $ABP = 100$ mmHg. The mean values of real data of all 14 subjects are given in Table 4.2. Shifting the mean value of the real data for use in HM has varying results for ARI. To study this effect, simulations were performed by only shifting the mean of real ABP in the range 60 to 140 mmHg, while other variables of HM, P_aCO_2 is kept at its baseline values, and EEG is kept at zero. This simulation gives the information about the autoregulatory capacity for only changes in ABP. The results are summarised in Table 5.2. Also shown in the table are the ARI values obtained when ARI is computed only for the real data of ABP and CBFV.

Fig 5.3 shows the boxplot of the ARI values of all subjects for varying mean ABP, where the red line in the middle of the box is the median value, and the bottom and top edges of the box indicate the 25th and 75th percentiles, respectively. The whiskers extend to the most extreme data points.

The results in Table 5.2 shows that for real data the regulation is good (around ARI of 3) or better (5 and above) in most of the subjects. When the real ABP data is shifted in mean and used as input in the HM on average there is an increase in ARI for an increase in mean ABP. This could be due to the fact that in the absence of changes in other confounding inputs (P_aCO_2 and EEG) the mean ABP becomes the dominant factor contributing to ARI. From Fig 5.3 it is clear that there is high variability in ARI at low values of mean ABP, and the variability reduces at higher mean ABP.

Subject	Real ABP	Mean ABP 60	Mean ABP 80	Mean ABP 100	Mean ABP 120	Mean ABP 140	Real ABP / CBFV
1	0.845	0	0.879	1.753	2.44	2.784	6
2	1.081	0.567	1.741	2.524	2.87	3.054	3.505
3	1.466	0.508	2.102	2.742	2.933	3.015	3.066
4	1.562	0.802	1.84	2.551	2.845	3.002	6.448
5	1.063	0	1.307	2.167	2.677	2.905	6.223
6	2.386	0.673	2.226	2.794	2.975	3.047	7.117
7	1.054	0	1.121	1.93	2.551	2.838	4.449
8	1.061	0.487	1.663	2.464	2.861	3.07	3.328
9	2.146	1.882	2.772	2.984	3.071	3.116	3.031
10	1.075	0	0.933	1.776	2.437	2.756	2.729
11	1.7	0	1.465	2.361	2.713	2.878	6.861
12	2.14	0.632	2.195	2.73	2.903	2.983	5.715
13	1.267	0	1.349	2.18	2.666	2.893	2.914
14	1.052	0	1.167	2.32	2.744	2.925	7.868

Table 5.2: *ARI* values of each subject when mean *ABP* is varied from 60 to 140 mmHg

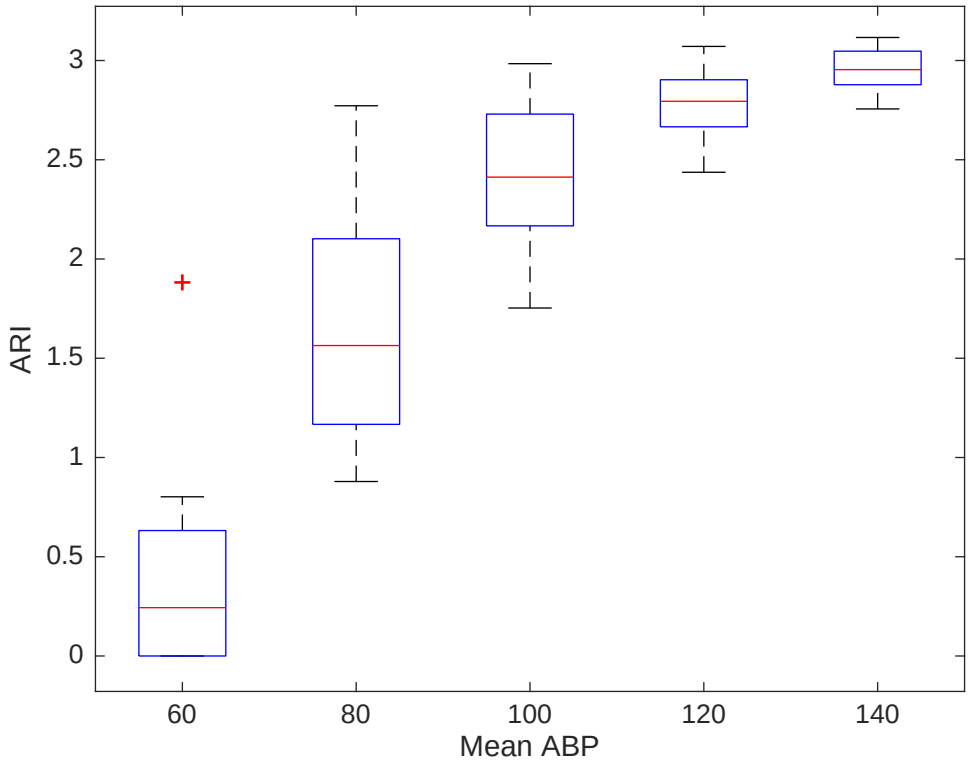

Figure 5.3: Range of *ARI* values for all 14 subjects, when mean *ABP* is increased from 60 to 140 mmHg, in steps of 20 mmHg

5.6 Results

All simulations were carried out with the mean of ABP shifted to 100 mmHg. The input EEG signals were generated using the NMM. From the output of the NMM, the first 5 secs were truncated so that any initial transients are removed. Then the DC value was removed using the mean of the signal, and the signals were scaled to 0.5 power by scaling the RMS value of the generated signal. The scaling was done so that the input remains similar to the magnitude that was used for the input stimulus u in HM. Shown in Table 4.3 are four different combinations of a different inputs, which are colour coded, and they can be considered as four cases for the ease of referring to the types of input combination used for a particular simulation.

For all the four cases the simulations were run for varying CBF % levels, a total of 8 levels from 100% to 30%, as shown in Table 4.4. In all individual simulations the output is the generated CBF. This generated CBF is them compared with modelled CBF from Tiecks model using the real ABP data as input into the Tiecks model, to calculate ARI values. For TFA the generated CBF is compared with real CBF data. The TFA analysis was carried out using the software created by CARNET group. From the TFA software output only the low frequency components of TFA (0.07 - 0.20 Hz) are considered here and among them only the TFA low frequency Gain and Phase only are considered and plotted as these two parameters are more commonly used measures. Table 5.3 shows the calculated ARI, TFA gain and TFA phase, all in the form of mean and standard deviation taken across thereafter of 14 subjects.

5.7 Discussion

In Figures 5.4, 5.5 and 5.6 the mean and standard deviation among the subjects are shown for the four cases for ARI, TFA Gain and TFA Phase. In this set of figures the EEG power is 0.5. In all the figures, considering each of the case individually and

Table of Mean and Standard Deviation for ARI, TFA Low Frequency Gain, TFA Low Frequency Phase																
CBF →	100		90		80		70		60		50		40		30	
Case ↓	Mean	SD	Mean	SD	Mean	SD	Mean	SD	Mean	SD	Mean	SD	Mean	SD	Mean	SD
ARI																
	1.68	0.66	1.43	0.55	1.23	0.44	0.98	0.32	0.57	0.20	0.00	0.00	0.00	0.00	0.00	0.00
	1.94	0.73	1.68	0.67	1.48	0.63	1.23	0.55	0.80	0.43	0.10	0.20	0.00	0.00	0.00	0.00
	1.66	0.62	1.43	0.52	1.12	0.34	0.89	0.27	0.49	0.17	0.00	0.00	0.00	0.00	0.00	0.00
	1.99	0.71	1.77	0.67	1.45	0.57	1.21	0.52	0.82	0.42	0.09	0.20	0.00	0.00	0.00	0.00
TFA Low Frequency Gain																
	0.29	0.01	0.26	0.01	0.23	0.01	0.20	0.00	0.16	0.00	0.11	0.00	0.07	0.00	0.05	0.00
	0.28	0.01	0.24	0.01	0.22	0.01	0.19	0.01	0.15	0.01	0.10	0.01	0.07	0.00	0.05	0.00
	0.28	0.00	0.25	0.00	0.22	0.00	0.19	0.00	0.15	0.00	0.11	0.00	0.07	0.00	0.05	0.00
	0.27	0.01	0.25	0.01	0.22	0.01	0.19	0.01	0.15	0.01	0.10	0.01	0.07	0.00	0.05	0.00
TFA Low Frequency Phase																
	20.24	0.85	10.67	0.54	4.60	0.43	-2.32	0.47	-11.41	0.62	-24.76	1.04	-30.77	0.99	-35.25	0.87
	18.90	1.70	9.47	1.84	3.62	1.93	-2.91	1.93	-11.36	1.99	-21.20	2.49	-23.41	4.83	-23.71	6.86
	19.15	0.63	10.80	0.88	3.36	0.79	-2.71	0.35	-11.26	1.36	-23.47	1.60	-29.50	2.46	-35.64	1.33
	18.81	1.08	10.57	1.36	3.05	1.11	-2.89	0.90	-10.94	1.53	-21.45	2.27	-23.06	4.27	-24.02	7.11

Table 5.3: Table showing mean and standard deviation of ARI, TFA Gain and TFA Phase

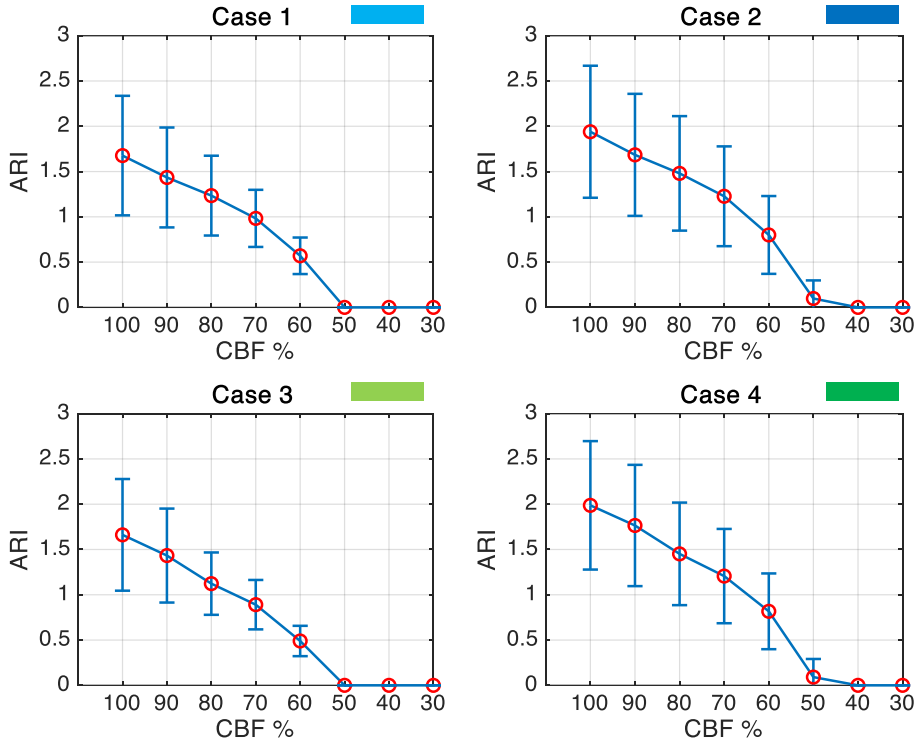

Figure 5.4: Mean values of ARI for all the subjects represented by `red´ circle, bars represent standard deviation

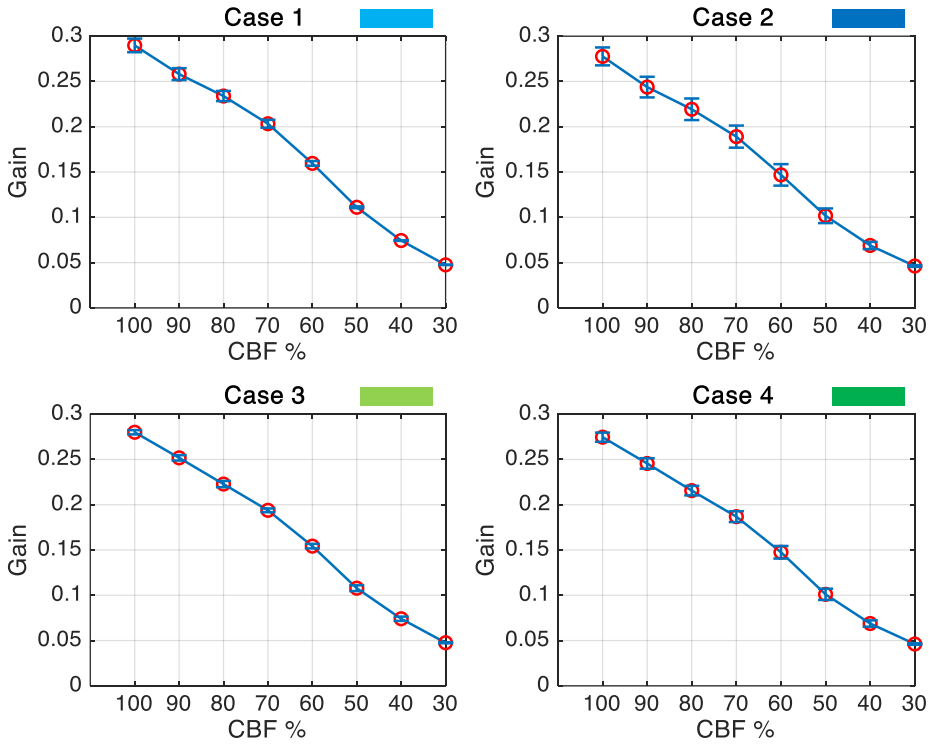

Figure 5.5: Mean values of TFA Gain for all the subjects represented by `red´ circle, bars represent standard deviation

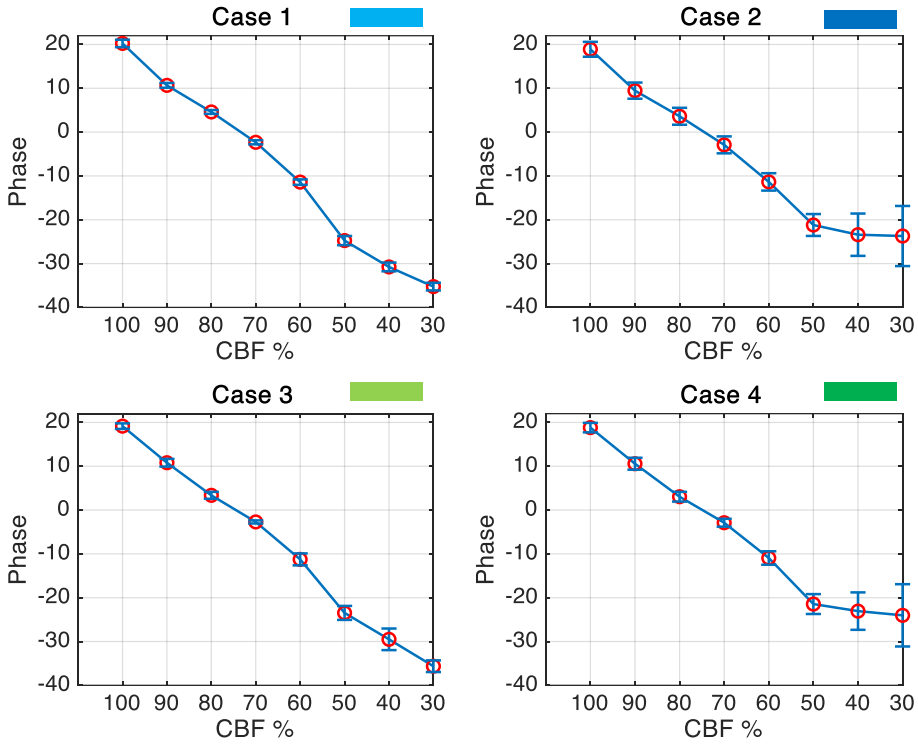

Figure 5.6: Mean values of TFA Phase for all the subjects represented by `red´ circle, bars represent standard deviation

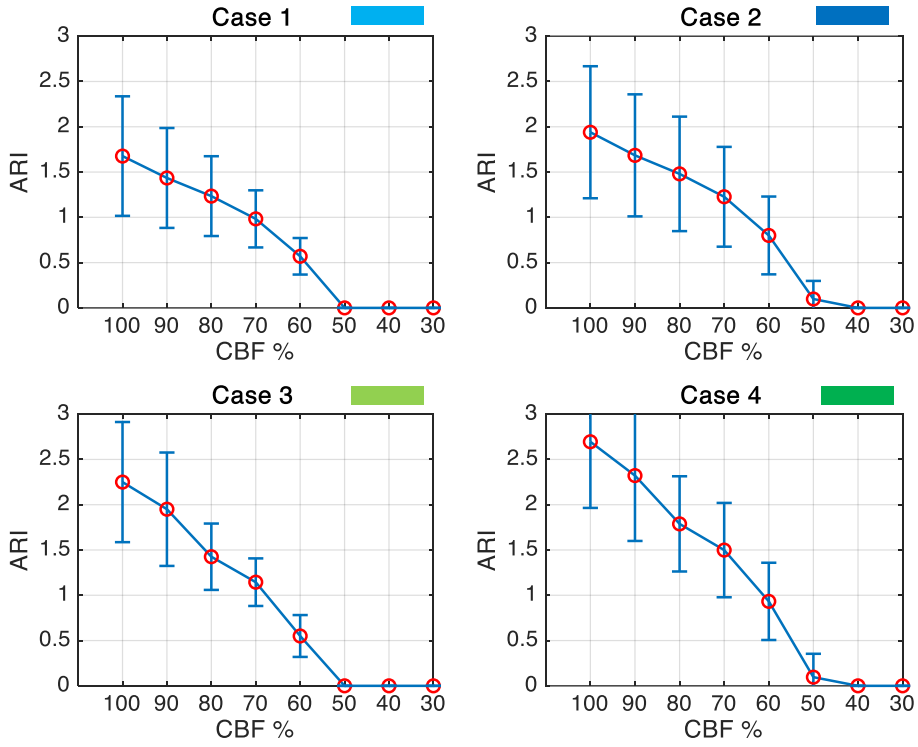

Figure 5.7: Mean values of ARI (Two fold EEG*2) for all the subjects represented by `red´ circle, bars represent standard deviation

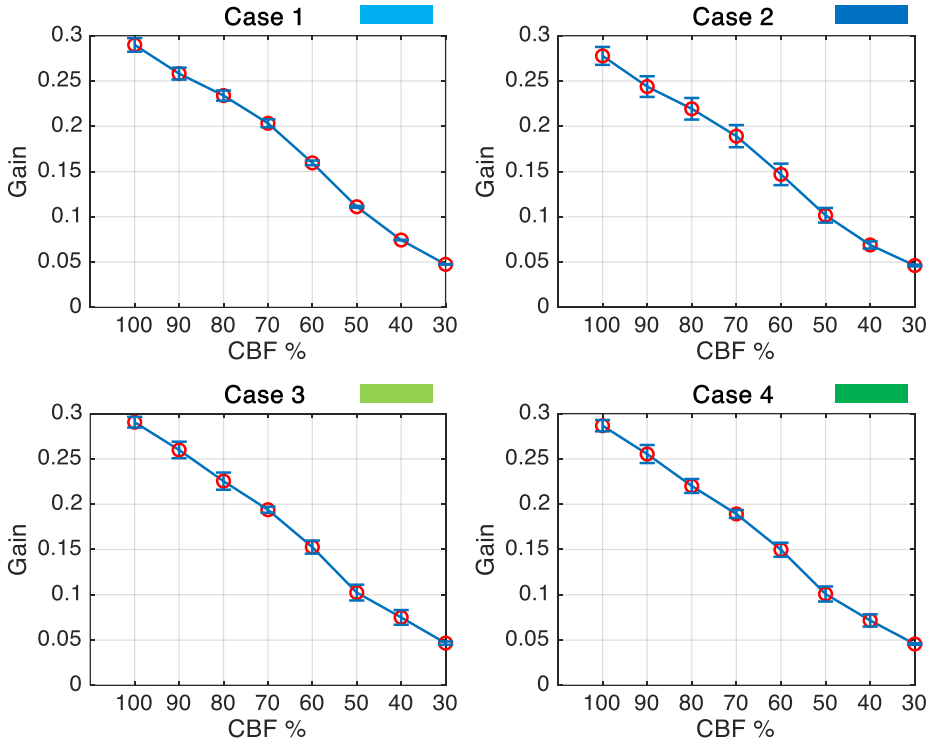

Figure 5.8: Mean values of TFA Gain (EEG*2) for all the subjects represented by `red´ circle, bars represent standard deviation

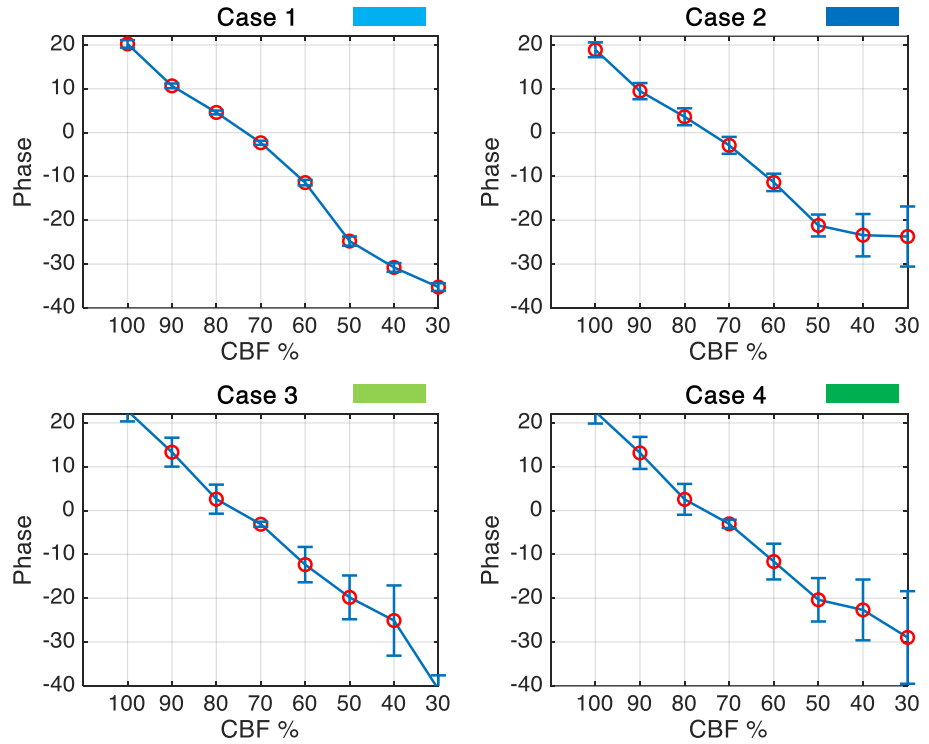

Figure 5.9: Mean values of TFA Phase (EEG*2) for all the subjects represented by `red´ circle, bars represent standard deviation

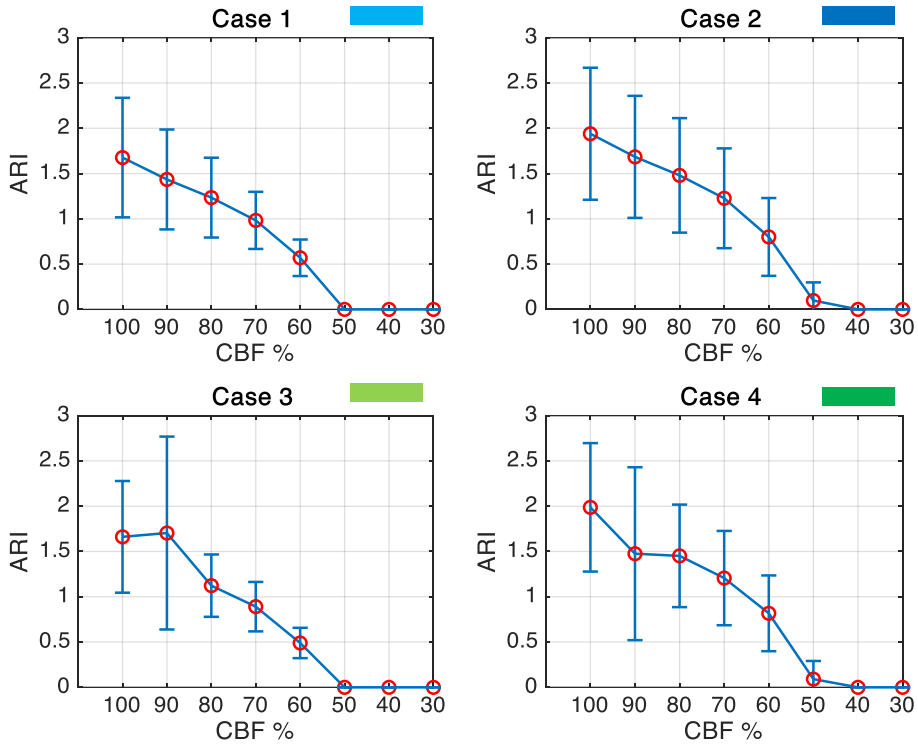

Figure 5.10: Mean values of *ARI* (*EEG* 19 Hz) for all the subjects represented by `red´ circle, bars represent standard deviation

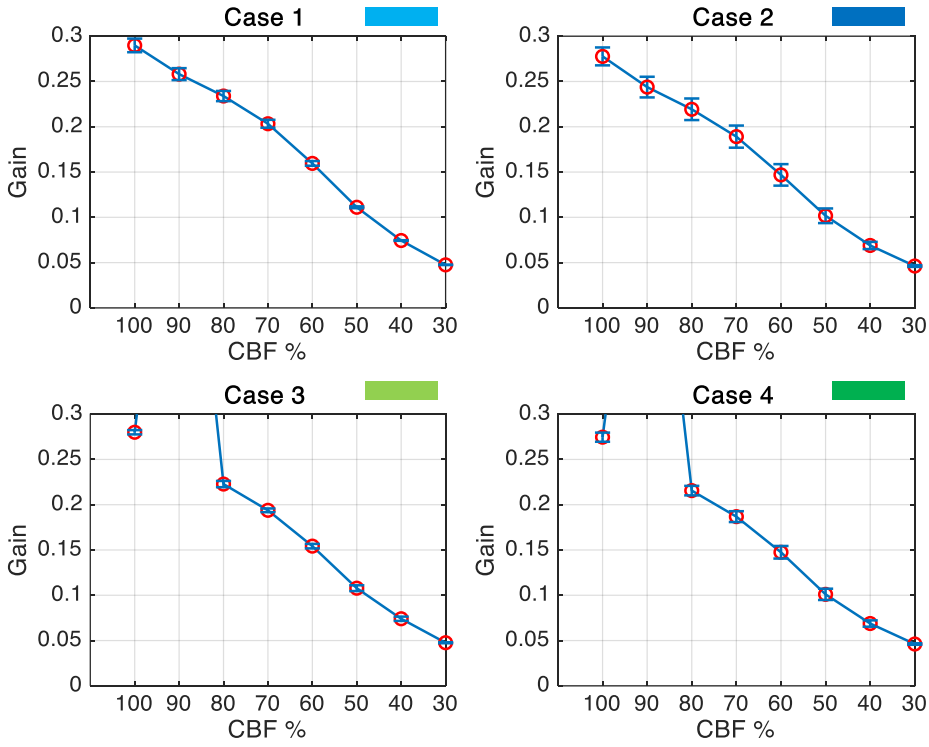

Figure 5.11: Mean values of *TFA* Gain (*EEG* 19 Hz) for all the subjects represented by `red´ circle, bars represent standard deviation

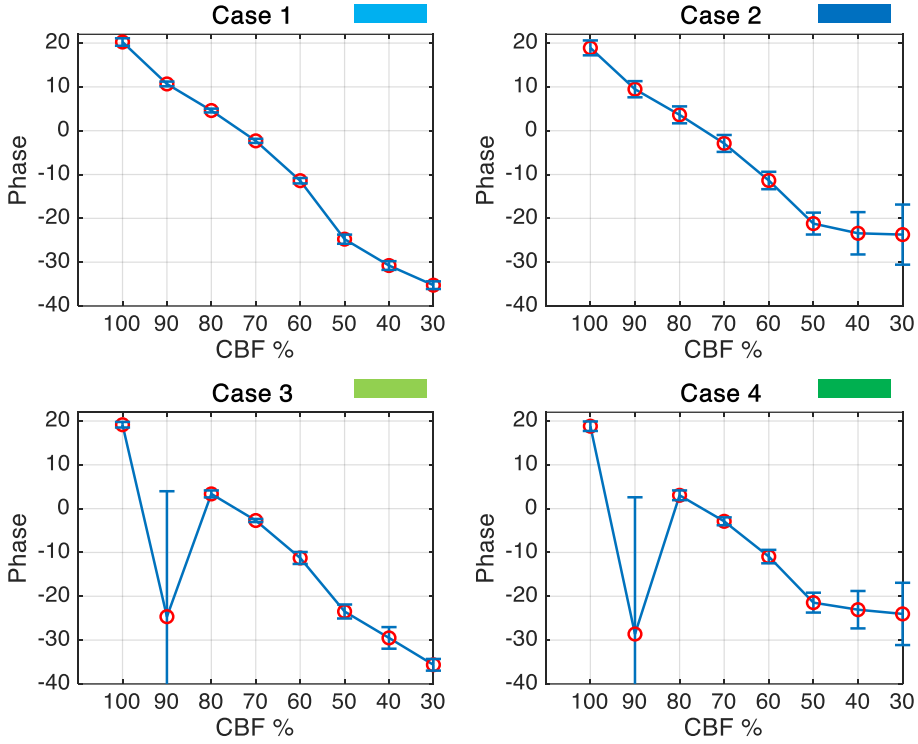

Figure 5.12: Mean values of TFA Phase (EEG 19 Hz) for all the subjects represented by `red´ circle, bars shows the standard deviation

also across different methods, the most obvious observation is the variability among subjects. The mean ARI values are bit higher in case 2 compared to case 1, the difference being caused due to the input in case 2, being the real data for P_aCO_2. The value of P_aCO_2 in case 1 is set to a constant of 40 mmHg, while in case 2, the average of mean P_aCO_2 is 36.80 mmHg. So on average the reduction in mean P_aCO_2 increases the ARI values, this shows the influence of P_aCO_2 on autoregulation strength. In case 3 and case 4, the EEG input is added and this causes the ARI to improve compared to that without EEG input. This applies for both with and without P_aCO_2.

In all the figures the variability among subjects also seems to decrease along with the reduction in CBF levels. The ARI values almost become zero when the CBF reduces below 50 % of normal flow. When P_aCO_2 is added, due to the low mean value of real P_aCO_2 compared to the assumed baseline, there is still some regulation preserved at 50 % reduced CBF and it too falls to zero at 40 % CBF. Similar to the

comparisons made with ARI, for TFA gain there is a small reduction in gain when real P_aCO_2 is added to the input. Then adding the EEG to the input reduces TFA gain by a small amount compared to that without EEG input. The reduction in TFA gain indicates that the autoregulation is improved (Van Beek et al., 2008). The more noticeable difference between TFA gain and the ARI method, is that in case of TFA gain, the variability between subjects is very low. This could mean that for the given data set, the TFA method shows less variability compared to ARI assessment method. The TFA phase plots shows that there is only a very small change between different cases; with real P_aCO_2 inputs the rate of fall in phase is slower.

In summary both ARI method and TFA method results show that P_aCO_2 increases autoregulation strength and when EEG input is added this increases further.

Figures 5.7, 5.8 and 5.9 shows the results when the input EEG power is increased from 0.5 to 2. The ARI values are increased compared to EEG with power 0.5. Comparing the TFA Gain between Fig 5.5 and 5.8, for case 3, gain is increased by a small amount when EEG power is increased. Similarly TFA phase also shows an increase of a small value.

In all these simulations the EEG input frequency was also reduced simultaneously while reducing CBF. In this study when an EEG frequency of 19 Hz was used for 90 percent CBF, the results seen in figures 5.10, 5.11 and 5.12 clearly show that the values of ARI, TFA gain and TFA phase all suddenly shoot up and then fall back to normal for the subsequent level of CBF. In order to inspect the behaviour observed while the EEG input frequency is 19 Hz, few signals with nearby frequencies were generated and the whole simulations were carried out. The results showed no abrupt changes in values as seen for 19 Hz. Hence this particular result obtained for 19 Hz could be an anomaly and at present there is no explanation for this specific observation. This may be taken as a study on it own and future work could be done to explain the behaviour.

5.8 Summary

In this chapter two methods, transfer function analysis and autoregulation index, for assessing autoregulation were detailed. Simulations and results from these methods were then presented. From the results for various settings of EEG, the effects it has on autoregulation were discussed. This study shows that input EEG improves the mean autoregulation values by small amount, with the effects varying between subjects.

Chapter 6

Conclusion

6.1 Summary

In this thesis the effect of EEG input on cerebral autoregulation assessment was studied using a haemodynamic model. The required EEG signals were generated using Jansen's neural mass model, as detailed in chapter 2. The haemodynamic model used for this study is different to other models, as this model allows simultaneous input of ABP and P_aCO_2 along with neural stimulation (EEG), as discussed in Chapter 3. Studies have shown that in clinical situations during ischaemia the frequency of EEG decreases when CBF decreases, as discussed in chapter 4. Methods to emulate CBF reduction using a haemodynamic model was presented, also parameters used in the neural mass model for generating EEG signals of decreasing frequency were discussed.

Using the real experimental data for ABP, P_aCO_2 and EEG signals as inputs, CBF was generated. In chapter 5, methods for assessment of autoregulation were presented. From the generated CBF and real data, autoregulation status was studied using transfer function and autoregulation Index methods. The results for various levels of EEG input were presented and discussed in chapter 5.

In summary the results show that the EEG input increases the autoregulation by a small amount. Yet there was high variability among the subject data. In

this study fourteen healthy subject data were used. Still the results across the two different methods used to assess showed the same found here i.e the EEG input does increase the autoregulation strength, despite the variability between subjects. More subject data measured under controlled conditions would be needed, however to further validate the findings in this study.

6.2 Limitations of this study

The models used, both Neural mass model and Haemodynamic model are both compact models. The Neural mass model is a lumped model of typical interactions of different neurons in cortical column. Many more complicated models based on this has been developed by different authors, extending it to multiple population of neurons. In the context of our study, the basic neural mass model serves the requirements. Similarly the Haemodynamic model used in this study has a simple feedback where all the three stimuli are linearly added. A more complex haemodynamic model which includes detailed models for different pathways is desirable. However this study is a first step in understanding how EEG affects the autoregulation assessment. One of the limitation of this study is the arbitrary assignment of EEG frequencies to various CBF levels. Studies could be carried out in future for specific frequency and continuous variation in CBF, instead of step reductions.

6.3 Future directions

The inspiration for this study was the evidence from clinical studies showing that EEG frequency decreases with decreasing CBF. If autoregulation status could be monitored continuously, it would be a very valuable tool in intensive care unit. For this the physiological link between EEG frequency change and CBF change needs to be fully established. The complete mechanisms of autoregulation itself are however not yet completely understood. To understand autoregulation, many studies have

developed haemodynamic models to reproduce the physiological observations. The model for mechanism of how CBF reduction affects the function of neurons leading to reduction in EEG frequencies need to established. This model could then be added as a feedback loop to existing haemodynamic model, that is capable of producing changes in EEG when CBF reduces. Then this model could be used to simulate the clinical findings of EEG and CBF relationship. The observation made in Chapter 5, figures 5.10, 5.11 and 5.12 remains to be inexplicable. Whether it is a chance anomaly or has real potential to provide a new insight into the haemodynamic model, could be carried out as a new study. The experimental data used in this study comes from laboratory settings of healthy subjects, but, in future, clinical data from intensive care units could be used to repeat the current study. This would provide further insights into the effect of EEG on assessment of cerebral autoregulation.

Bibliography

Attwell, D., Iadecola, C., 2002. The neural basis of functional brain imaging signals. Trends in Neurosciences 25 (12), 621–625.

Attwell, D., Laughlin, S. B., 2001. An energy budget for signaling in the grey matter of the brain. Journal of Cerebral Blood Flow & Metabolism 21 (10), 1133–1145.

Babajani, A., Soltanian-Zadeh, H., 2006. Integrated MEG/EEG and fMRI model based on neural masses. Biomedical Engineering, IEEE Transactions on 53 (9), 1794–1801.

Barker, R. A., Cicchetti, F., Robinson, E. S., 2017. Neuroanatomy and Neuroscience at a Glance. John Wiley & Sons.

Bear, M. F., Connors, B. W., Paradiso, M. A., 2007. Neuroscience. Vol. 2. Lippincott Williams & Wilkins.

Blaber, A. P., Bondar, R. L., Stein, F., Dunphy, P. T., Moradshahi, P., Kassam, M. S., Freeman, R., 1997. Transfer function analysis of cerebral autoregulation dynamics in autonomic failure patients. Stroke 28 (9), 1686–1692.

Braitenberg, V., Schüz, A., 2013. Cortex: statistics and geometry of neuronal connectivity. Springer Science & Business Media.

Cipolla, M. J., 2009. Control of cerebral blood flow. In: The cerebral circulation. Morgan & Claypool Life Sciences.

Claassen, J. A., Meel-van den Abeelen, A. S., Simpson, D. M., Panerai, R. B., (CARNet), I. C. A. R. N., 2016. Transfer function analysis of dynamic cerebral autoregulation: a white paper from the international cerebral autoregulation research network. Journal of Cerebral Blood Flow & Metabolism 36 (4), 665–680.

da Silva, F. L., 2004. Functional localization of brain sources using eeg and/or meg data: volume conductor and source models. Magnetic resonance imaging 22 (10), 1533–1538.

David, O., Friston, K. J., 2003. A neural mass model for meg/eeg:: coupling and neuronal dynamics. NeuroImage 20 (3), 1743–1755.

Foreman, B., Claassen, J., 2012. Quantitative eeg for the detection of brain ischemia. Critical care 16 (2), 216.

Freeman, W. J., 1987. Simulation of chaotic eeg patterns with a dynamic model of the olfactory system. Biological cybernetics 56 (2-3), 139–150.

Freeman, W. J., et al., 1975. Mass action in the nervous system. Vol. 2004. Citeseer.

Friedman, D., Claassen, J., Hirsch, L. J., 2009. Continuous electroencephalogram monitoring in the intensive care unit. Anesthesia & Analgesia 109 (2), 506–523.

Friston, K. J., Mechelli, A., Turner, R., Price, C. J., 2000. Nonlinear responses in fmri: the balloon model, volterra kernels, and other hemodynamics. NeuroImage 12 (4), 466–477.

Giulioni, M., Ursino, M., 1996. Impact of cerebral perfusion pressure and autoregulation on intracranial dynamics: a modeling study. Neurosurgery 39 (5), 1005–1015.

Gonzalez, M., Quiles, M., Pulido, N., Garcia-Sola, R., Salvador, C., 1994. Intracranial pressure dynamics in clinical practice: online pc-based icp monitoring system. Medical and Biological Engineering and Computing 32 (5), 512–520.

Gonzalez, R., 2006. Imaging-guided acute ischemic stroke therapy: from time is brain to physiology is brain. American Journal of Neuroradiology 27 (4), 728–735.

Grimbert, F., Faugeras, O., 2006. Analysis of jansen's model of a single cortical column.

Hofmeijer, J., van Putten, M. J., 2012. Ischemic cerebral damage: an appraisal of synaptic failure. Stroke 43 (2), 607–615.

Hoge, R. D., Atkinson, J., Gill, B., Crelier, G. R., Marrett, S., Pike, G. B., 1999. Investigation of bold signal dependence on cerebral blood flow and oxygen consumption: the deoxyhemoglobin dilution model. Magnetic Resonance in Medicine: An Official Journal of the International Society for Magnetic Resonance in Medicine 42 (5), 849–863.

Huttmann, S. E., Windisch, W., Storre, J. H., 2014. Techniques for the measurement and monitoring of carbon dioxide in the blood. Annals of the American Thoracic Society 11 (4), 645–652.

Jansen, B. H., Rit, V. G., 1995. Electroencephalogram and visual evoked potential generation in a mathematical model of coupled cortical columns. Biological cybernetics 73 (4), 357–366.

Jansen, B. H., Zouridakis, G., Brandt, M. E., 1993. A neurophysiologically-based mathematical model of flash visual evoked potentials. Biological cybernetics 68 (3), 275–283.

Jones, E. G., Peters, A., 2012. Cerebral cortex: comparative structure and evolution of cerebral cortex. Vol. 8. Springer Science & Business Media.

Jordan, J. D., Powers, W. J., 2012. Cerebral autoregulation and acute ischemic stroke. American journal of hypertension 25 (9), 946–950.

Kandel, E. R., Schwartz, J. H., Jessell, T. M., of Biochemistry, D., Jessell, M. B. T., Siegelbaum, S., Hudspeth, A., 2000. Principles of neural science. Vol. 4. McGraw-hill New York.

Klein, S. P., Depreitere, B., Meyfroidt, G., 2019. How i monitor cerebral autoregulation.

Liu, X., Czosnyka, M., Donnelly, J., Budohoski, K. P., Varsos, G. V., Nasr, N., Brady, K. M., Reinhard, M., Hutchinson, P. J., Smielewski, P., 2015. Comparison of frequency and time domain methods of assessment of cerebral autoregulation in traumatic brain injury. Journal of Cerebral Blood Flow & Metabolism 35 (2), 248–256.

Logothetis, N., 2003. MR imaging in the non-human primate: studies of function and of dynamic connectivity. Current opinion in neurobiology 13 (5), 630–642.

Lopes da Silva, F., Hoeks, A., Smits, H., Zetterberg, L., 1974. Model of brain rhythmic activity. Biological Cybernetics 15 (1), 27–37.

McSwain, S. D., Hamel, D. S., Smith, P. B., Gentile, M. A., Srinivasan, S., Meliones, J. N., Cheifetz, I. M., 2010. End-tidal and arterial carbon dioxide measurements correlate across all levels of physiologic dead space. Respiratory care 55 (3), 288–293.

Mitsis, G. D., Ainslie, P. N., Poulin, M. J., Robbins, P. A., Marmarelis, V. Z., 2004. Nonlinear modeling of the dynamic effects of arterial pressure and blood gas variations on cerebral blood flow in healthy humans. In: Post-genomic perspectives in modeling and control of breathing. Springer, pp. 259–265.

Mountcastle, V. B., 1957. Modality and topographic properties of single neurons of cat's somatic sensory cortex. Journal of neurophysiology 20 (4), 408–434.

Noback, C. R., Ruggiero, D. A., Demarest, R. J., Strominger, N. L., 2005. The human nervous system: structure and function. Springer Science & Business Media.

Nolte, J., 2008. The Human Brain E-Book: An Introduction to its Functional Anatomy With STUDENT CONSULT Online Access. Elsevier Health Sciences.

Payne, S., 2006. A model of the interaction between autoregulation and neural activation in the brain. Mathematical biosciences 204 (2), 260–281.

Payne, S., 2016. Cerebral autoregulation: control of blood flow in the brain. Springer.

Payne, S., 2017. Cerebral Blood Flow and Metabolism: A Quantitative Approach. World Scientific.

Poulin, M. J., Robbins, P. A., 1996. Indexes of flow and cross-sectional area of the middle cerebral artery using doppler ultrasound during hypoxia and hypercapnia in humans. Stroke 27 (12), 2244–2250.

Reivich, M., 1964. Arterial pco2 and cerebral hemodynamics. American Journal of Physiology-Legacy Content 206 (1), 25–35.

Sanders, M. L., Elting, J. W. J., Panerai, R. B., Aries, M., Bor-Seng-Shu, E., Caicedo, A., Chacon, M., Gommer, E. D., Van Huffel, S., Jara, et al., 2019. Dynamic cerebral autoregulation reproducibility is affected by physiological variability. Frontiers in physiology 10, 865.

Sharbrough, F. W., Messick JR, J. M., Sundt JR, T. M., 1973. Correlation of continuous electroencephalograms with cerebral blood flow measurements during carotid endarterectomy. Stroke 4 (4), 674–683.

Shardlow, E., Jackson, A., 2011. Cerebral blood flow and intracranial pressure. Anaesthesia & Intensive Care Medicine 12 (5), 220–223.

Simpson, D., 2015. Cerebral autoregulation network. `http://www.car-net.org/content/resources`, (Accessed on 10/25/2019).

Steiner, L., Andrews, P., 2006. Monitoring the injured brain: Icp and cbf. BJA: British Journal of Anaesthesia 97 (1), 26–38.

Tameem, A., Krovvidi, H., 2013. Cerebral physiology. Continuing Education in Anaesthesia, Critical Care & Pain 13 (4), 113–118.

Tiecks, F. P., Lam, A. M., Aaslid, R., Newell, D. W., 1995. Comparison of static and dynamic cerebral autoregulation measurements. Stroke 26 (6), 1014–1019.

Ursino, M., Lodi, C. A., 1997. A simple mathematical model of the interaction between intracranial pressure and cerebral hemodynamics. Journal of Applied Physiology 82 (4), 1256–1269.

Ursino, M., Lodi, C. A., 1998. Interaction among autoregulation, co2 reactivity, and intracranial pressure: a mathematical model. American Journal of Physiology-Heart and Circulatory Physiology 274 (5), H1715–H1728.

Ursino, M., Ter Minassian, A., Lodi, C., Beydon, L., 2000. Cerebral hemodynamics during arterial and co2 pressure changes: in vivo prediction by a mathematical model. American Journal of Physiology-Heart and Circulatory Physiology 279 (5), H2439–H2455.

Van Beek, A. H., Claassen, J. A., Rikkert, M. G. O., Jansen, R. W., 2008. Cerebral autoregulation: an overview of current concepts and methodology with special focus on the elderly. Journal of Cerebral Blood Flow & Metabolism 28 (6), 1071–1085.

van Rotterdam, A., Da Silva, F. L., Van den Ende, J., Viergever, M., Hermans, A., 1982. A model of the spatial-temporal characteristics of the alpha rhythm. Bulletin of mathematical biology 44 (2), 283–305.

Whittington, M. A., Traub, R., Kopell, N., Ermentrout, B., Buhl, E., 2000. Inhibition-based rhythms: experimental and mathematical observations on network dynamics. International journal of psychophysiology 38 (3), 315–336.

Willie, C. K., Tzeng, Y.-C., Fisher, J. A., Ainslie, P. N., 2014. Integrative regulation of human brain blood flow. The Journal of physiology 592 (5), 841–859.